Tuning the electronic and structural properties of Gd-TiO$_2$-GO nanocomposites for enhancing photodegradation of IC dye: The role of Gd^{3+} ion

Samuel Osei-Bonsu Oppong, Francis Opoku, Penny Poomani Govender*

Department of Applied Chemistry, University of Johannesburg, P.O. Box 17011, Doornfontein Campus, 2028, Johannesburg, South Africa

ARTICLE INFO

ABSTRACT

In recent years, there has been a growing interest in developing highly efficient photocatalysts with a visible light active semiconductor as one of its components. Herein, visible-light-driven photocatalytic activity of Gd-TiO$_2$-GO nanocomposites were fabricated by sol–gel method. The photocatalytic property was evaluated for photodegradation of indigo carmine (IC) dye. The structural properties of the fabricated samples were characterised using SEM, XRD, PL, TEM, Raman, BET, EDS, elemental mapping and XPS analysis. To provide further insights into the synergistic effect, a hybrid density functional theory calculation was used to study the charge transfer, electronic and structural properties of Gd–TiO$_2$–GO nanocomposite. The as-fabricated nanocomposites showed improved visible light photocatalytic performance and degradation efficiency over pure TiO$_2$. The optimal Gd content was found to be 0.6 wt%, and the apparent pseudo-first order photodegradation rate of IC dye was 14.19-fold higher than that of pure TiO$_2$ nanoparticles under visible–light irradiation. Moreover, hydroxide radicals and holes were the main active species, and the hybrid nanocomposites exhibited high stability and recyclability during the IC dye degradation process. Herein, both GO sheets and Gd^{3+} ion were excellent co-catalysts and their presence promote the reaction sites and synergistically enhanced the photocatalytic degradation of IC dye. Also, the smaller effective mass caused a high separation of photogenerated charge carriers, thereby promoting the photodegradation efficiency. This work offers a new understanding of designing high-performance TiO$_2$-based photocatalysts for wastewater treatment.

1. Introduction

In the last decade, researchers in water industries around the globe have been trying to develop novel strategies for degrading organic pollutants in water using semiconductor materials through the process of photocatalysis [1]. About 2.6 billion people had been reported to have died from infectious diseases resulting from improper sanitation practices and lack of potable water [2]. Again, it has been reported that water supply is predicted to decline with population growth in the near future, even in areas considered to be water–rich [1]. Documented reports have also shown that our water bodies are being polluted due to population increase, dumping of the industrial chemical by–products, organic matter and pesticides run–off into water bodies by agriculture practices [3]. Conventional techniques, such as coagulation/flocculation, electrolyte decomposition, nanofiltration, oxidation, biological treatment and activated carbon [4,5], which were previously employed for solving global pollution problems, have proven to be ineffective due

to the generation of a large volume of sludge, incomplete organic pollutant degradation, as well as high operational cost [6]. This has prompted researchers to search for an alternative technique to eliminate organic pollutants in water bodies. Nowadays, employing semiconductor–based photocatalysis to eradicate organic pollutants in water bodies has been a favourable technology due to its non–toxicity, economical and efficient mineralisation of pollutants [7]. Thus, photocatalysis has proven to possess an effective ability to mineralise the complex pollutants to fairly less harmful compounds, such as H$_2$O and CO$_2$ [8].

Semiconductor materials, including ZnO, TiO$_2$, ZnS, CdS and ZrO$_2$ have been broadly explored owing to its unique chemical and electronic structure, good photocatalytic activities and favourable charge transport behaviour [9]. Among the well–known semiconductor, anatase TiO$_2$ is the most efficient photocatalyst owing to its captivating properties including excellent degradation capacity, low cost, biocompatibility, non–toxicity, photostability and capable of accelerating the

---

* Corresponding author.
  E-mail addresses: samkello2002@yahoo.com (S.O.-B. Oppong), fopoku@uj.ac.za (F. Opoku), pennyg@uj.ac.za (P.P. Govender).

oxidation of organic pollutants in water [10]. Moreover, TiO_2 has shown to possess extensive applications in many research areas, such as photochromism, photocatalysis, gas sensors, manufacturing of printing ink, self–cleaning ceramics, glass coating and photovoltaics [11]. Besides, TiO_2 has been used as additives in most food, consumer and personal care products [12]. However, two crucial problems restrict its practical applications as a photocatalyst. This includes larger bandgap energy and fast recombination of charge carriers, which impedes its operation in the visible light region, thereby reducing the photoactivity [13]. Therefore, there is the need to develop a hybrid material that would make TiO_2 photocatalyst having a suitable visible light sensitivity, efficient charge carrier separation and enhanced photocatalytic performance.

Recent reports on a TiO_2 modification to enhance its photodegradation showed that modifying it with non–metals or metals could increase its visible light absorptivity and promote its charge carrier separation, thereby increasing the photoactivity. Previous studies have revealed that doping semiconductor–based photocatalyst with a suitable quantity of transition metal prevents the electron–hole pair's recombination [14,15]. Earlier studies had revealed that modifying TiO_2 with rare–earth metals (Ce^{3+}, Dy^{3+}, Nd^{3+}, Sm^{3+}, La^{3+}) [16] could delay the recombination of charge carriers and subsequently, boost the degradation of pollutants in aqueous solution compared with the pure TiO_2. The scavenging nature of rare earth metal ions has been shown to be accountable for the reduced recombination rate of charge carriers. The behaviour of rare earth metal ions towards photodegradation of pollutants was due to its ability to form a complex with a range of contaminants by interacting with the functional groups of the f–orbital of the rare earth metal ions. This property has demonstrated to offer an efficient way to concentrate the pollutants on the exterior of the semiconductor.

Other factors that promote the photoactivity of TiO_2 include noble metal deposition, combining with another semiconductor or modifying it with carbon materials [17,18]. Carbon–based nanomaterials, such as graphene have proven to be a potential material in nanotechnology owing to its outstanding characteristics, such as efficient migration of charge carriers, large exposed area, better electron conductivity and unique two–dimensional (2D) structure [19–21]. For example, graphene–based photocatalyst had been employed to degrade organic pollutants in water and splitting water into hydrogen gas [22–25]. Recent studies on GO have shown that it has a lot of advantages over graphene due to its unique characteristics, such as high transparency, effective corrosion resistance, excellent stability and efficient electronic properties. Besides, the oxygen–containing functional group of GO sheets have also been observed to enhance the hydrophilic property of the photocatalyst [15], thereby making it a suitable medium to support the nanocomposite [26]. Further studies have revealed that GO can act as a photosensitiser and an electron sinker to inhibit electron–hole pairs recombination, thereby improving the photodegradation efficiency of organic pollutants [15].

Recent efforts towards the design of GO nanocomposites photocatalysts for the degradation of various pollutants have been reported [27–29]. To the best of our knowledge, the decoration of Gd–TiO_2 nanostructure on GO sheets for the photodegradation of indigo carmine (IC) dye under light irradiation is limited. Graphene materials, including graphene oxide and reduced graphene oxide, are well known as efficient cocatalysts for semiconductor photocatalyst. Graphene oxide has received a great deal of attention for environmental applications due to its lightweight and possesses a large amount of delocalised electrons. Moreover, visible light absorption of graphene oxide was more reduced than graphene, which could favour visible light irradiation on the TiO_2 surface. Therefore, graphene oxide with a unique specific surface area, high charge carrier mobility and electron conductivity was employed as semiconductor photosensitisers to harvest the solar energy and enhance the separation of charge carriers. Moreover, Gd^{3+} ion functions as an electron reservoir to promote the charge

transfer and offered reactive sites for efficient photodegradation of IC dye. Thus, designing a hybrid nanocomposite composed of graphene oxide, Gd^{3+} ion and TiO_2 for highly enhanced photocatalytic activity is reasonable and attractive. Studies for the photocatalytic stability and degree of degradation of IC dye by Gd–TiO_2–GO photocatalyst were also assessed. To access the underlying mechanism of the photocatalytic enhancement and charge transfer from a theoretical perspective, first–principles calculation was used. Here, interfacial interaction, structural stability and electronic property of Gd–TiO_2–GO nanocomposite was systematically studied *via* a hybrid density functional theory (DFT) calculation. The theoretical calculation can provide insights into the experimental results and may support the future development of TiO_2–based photocatalyst materials.

2. Experimental

2.1. Materials and reagents

All the chemicals were procured from Sigma–Aldrich and used without further purification. Deionised water was used throughout the experiment.

2.2. Synthesis of graphene oxide (GO)

The fabrication of GO, which employed the modified Hummers method [30] was prepared according to our earlier report [31]. In this method, 15 g of $KMnO_4$ was added to 5 g of graphite contained in a 500 mL round bottom flask, and the resulting mixture was stirred to form a homogeneous mixture. The mixture was then placed in an ice water bath and a concentrated mixture of H_2SO_4 (360 mL)/H_3PO_4 (40 mL) was added with vigorous stirring until a uniform liquid paste was formed. The reaction mixture was heated to 50 °C and stirring was continued for a further 12 h before being allowed to cool to room temperature. A volume of 400 mL of deionised water and 5 mL H_2O_2 (30%) was added slowly, followed by rapid stirring to prevent effervescing. Thereafter, centrifugation (7500 rpm for 20 min at 5 °C) of the solution was undertaken to remove impurities. The remaining solid material was washed with deionised water and HCl (30%), followed by centrifugation. The solid material was changed to a semi–solid state by immersing the material in 200 mL petroleum ether, and later filtered *via* a Teflon membrane (1 µm pore). Finally, the isolated solid was vacuum dried overnight at room temperature.

2.3. Preparation of Gd–TiO_2–GO photocatalyst using sol–gel method

Gd–TiO_2–GO photocatalyst was prepared by adding 5 mL of Ti(OCH $(CH_3)_2)_4$ to a 50 mL absolute ethanol and magnetically stirred for about 30 min to attain a uniform mixture. About 0.3, 0.6 and 1.0% of Gd $(NO_3)_3 \cdot 6H_2O$ and a 0.5% GO were subsequently added to the mixture with continuous stirring for about 1 h. Polyethylene glycol (2 mL) was added to the resultant solution and further stirred for another 30 min. In addition, deionised water (10 mL) was added slowly while stirring continuously to obtain the gel, which was then separated by centrifugation after severally rinsed with deionised water and ethanol. The obtained sample was dried at 60 °C for 24 h and then characterised. Titania or Titania–graphene oxide was also prepared using the same procedure without the addition of either both GO and Gd$(NO_3)_3 \cdot 6H_2O$ or only Gd$(NO_3)_3 \cdot 6H_2O$, respectively.

2.4. An experiment for the photocatalytic activity

For the photocatalytic degradation reaction, a Full–Spectrum Solar Simulator (Newport, Model: 9600) was employed. The solar simulator was equipped with 150 W ozone free xenon lamp, where a collimated beam of 33 mm diameter, which is an equivalent of 1.3 suns was produced. Since the photocatalytic degradation experiment was carried out

under visible light irradiation, a spectrophotometer (Shimadzu UV–2450) was employed to assess the concentration of the residual IC solution at a wavelength of 610 nm. In this process, 100 mg of the photocatalyst was suspended in an aqueous solution of 20 mg/L of IC dye and then magnetically stirred in the dark, prior to irradiation, for 1 h and at 25 C in a quartz beaker (150 mL) and this was carried out to create an adsorption equilibrium of IC dye with the semiconductor photocatalyst. After the adsorption equilibrium, the light sources were switched on for photodegradation of IC dye at 30 min intervals by the various photocatalysts and aliquots (5 mL) was withdrawn from the solution using a disposal syringe containing filtered membrane of 4 μm for a period of 210 min. The percentage (%) degraded IC dye solution was evaluated following Eq. (1):

$$\% \, degraded \quad IC \quad dye \quad solution = \frac{C_o - C_t}{C_o} x \, 100 \tag{1}$$

where C_o and C_t are the initial concentration and concentration after the time t of IC dye.

2.5. Characterisation

The morphology, microstructure and crystal phase of the as–fabricated photocatalysts were characterised by X–ray diffractometer (Philip's X–ray diffraction) at 30 mA and 40 kV. Perkin Elmer Raman microscope (Raman Micro 200) and Perkin Elmer Fourier–transform infrared spectroscopy (FTIR) spectrometer (Spectrum 100) were used to record the Raman and FTIR spectra, respectively. The surface morphology and the size and internal morphology of the as–prepared photocatalysts were evaluated using the scanning electron microscopy (SEM) on TESCAN (Vega 3XMU) and transmission electron spectroscopy (TEM) (JEOL, Model: JEM-2100F), respectively. The Energy dispersive spectroscopy (EDS) attached to SEM was used to study the elemental compositions of the samples. Brunauer–Emmett–Teller (BET) measurements were assessed using Micrometrics ASAP 2020 V4.00. The optical analysis was assessed with UV–vis diffuse reflectance spectroscopy (DRS) on UV–2540 Shimadzu instruments using BaSO₄ as the reflectance standard.

2.6. Density functional theory calculations

The theoretical calculation was carried out by a plane–wave DFT method as implemented in the Cambridge Serial Total Energy code [32] of Materials Studio 2016 [33]. The generalized gradient approximation (GGA) of the Perdew–Burke–Ernzerhof (PBE) functional [34] was used to describe the exchange–correlation potential. The norm conserving pseudopotential approach was employed to treat the ion–electron interactions [35]. The energy cut–off and convergence criteria for force and energy was set at 500 eV, 0.01 eV/Å and 10^{-6} eV/atom, respectively, using the conjugate gradient method [36]. A relatively large vacuum space of 20 Å was used to reduce the interactions and artificial dipole moments between the neighbouring slabs. The Monkhorst–Pack with k–point grids of $12 \times 12 \times 1$, $12 \times 1 \times 1$ and $6 \times 1 \times 1$ were used to sample the Brillouin zones of GO sheet, pure TiO₂ and the TiO₂–GO and Gd–TiO₂–GO nanocomposites [37]. Since the GGA–PBE functional underestimate the bandgap of most semiconductors [38], the hybrid Heyd–Scuseria–Ernzerhof (HSE06) functional [39] was employed to obtain more accurate electronic properties and structural stability.

3. Results and discussion

3.1. FTIR analysis

The FTIR spectra obtained from the synthesised TiO₂, TiO₂–GO and Gd–TiO₂–GO composites with varying concentrations of Gd are given in Fig. 1.
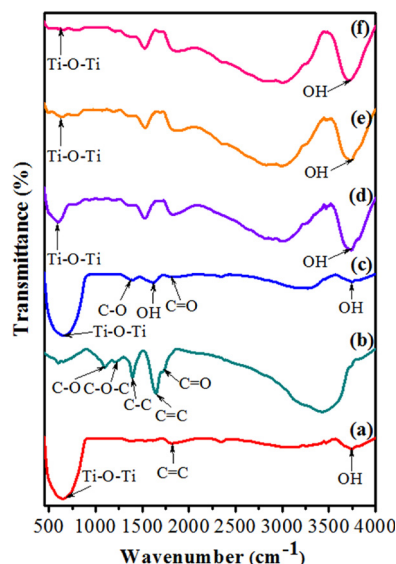

Fig. 1. FTIR spectra of (a) pure TiO₂, (b) GO sheets, (c) TiO₂–GO, (d) Gd–TiO₂–GO (0.3% Gd), (e) Gd–TiO₂–GO (0.6% Gd) and (f) Gd–TiO₂–GO (1.0% Gd) nanocomposite.

The two observed peaks situated at 1632 and 3600 cm⁻¹ corresponded to the OH bending and stretching vibrations of the adsorbed water molecules from the OH group, respectively [40]. The nanocomposite ability to absorb water is vital to form the hydroxide (HO˙) radicals during the redox reaction. The spectrum for GO sheets showed a broad absorption peak at 3415, 1732 and 1621 cm⁻¹, which was attributed to the O−H stretching vibration, carboxyl C═O stretching and aromatic C═C stretching, respectively. The peak located at 1055 and 1420 cm⁻¹ were ascribed to the C−O epoxy group positioned at the edges of the GO sheets and carboxyl OH stretching, respectively [41]. For the Gd–TiO₂–GO nanocomposites, the peaks assigned in the range of 1300–1000, 1680–1450, 1720–1706 and ~1384 cm⁻¹ were due to C−O stretching vibration, C═C stretching vibration from oxidised graphite domains, C═O stretching and C−H bending vibrations. The peak at 1000 cm⁻¹ were as a result of the combination of Ti−O−C and Ti−O−Ti vibrations [42]. The Ti−O−C vibration showed that there was a strong bonding between GO and TiO₂. The peaks located between ~664 to ~723 cm⁻¹ might be ascribed to the modification of Gd³⁺ ion. There were no peaks found around 1389 cm⁻¹ and this might be attributed to the C−H bending vibration in the nanocomposite [16]. Again, no peak of alkoxy residue confirmed the absence of impurity in the nanocomposite after calcination.

3.2. XRD analysis

The crystal structure of the as–synthesised nanocomposite was evaluated via X–ray diffraction. Crystalline nanoparticle structures have been reported to be an efficient photocatalyst than amorphous materials. The XRD patterns of TiO₂, TiO₂–GO, Gd–TiO₂–GO nanocomposites (with varying concentrations of Gd), as well as its detail corresponding peaks inferring that they all are crystalline, see Fig. 2.

The observed peaks at 25.4, 38.1, 43.3, 54.2, 55.3, 62.9 and 75.4 cm⁻¹ agreed with the anatase phase of TiO₂ and hence, corresponded to the (101), (004), (002), (105), (211), (204) and (215) crystal planes, respectively [43]. The GO sheets showed an XRD peak at 2θ = 10° with a d–spacing of 0.85 nm, which agreed to the (002) plane [41]. This was much larger compared to the interlayer spacing of 0.34 nm for pristine graphite [44]. The increase in d–spacing was ascribed to the introduced oxygen functional groups on the parent graphite surface and the separation of graphene into GO [45]. Low peaks for Gd₂O₃ and GO were found on the crystal structure of the
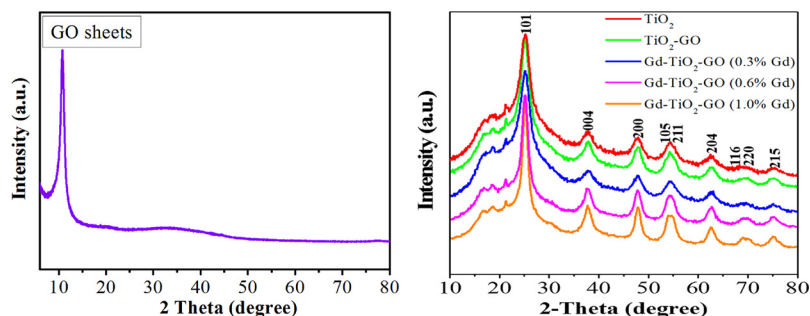
Fig. 2. XRD patterns of GO sheets, pure TiO_2, TiO_2–GO and Gd–TiO_2–GO nanocomposites with variable concentrations of Gd.

nanocomposites owing to their low concentrations compared to TiO_2. Besides, there was also no major observable peak to GO sheets in the TiO_2–GO nanocomposite due to its low amount [46]. The Debye–Scherer equation [18] was used to evaluate the average particle size, which was found to be between 9 and 16 nm using the (101) peak. The particle size was calculated according to Eq. (2):

$$D = \frac{k\lambda}{\beta \mathrm{Cos}\theta} \tag{2}$$

where λ is the wavelength of XRD pattern, D denotes crystal size of the nanocomposite, β refers to the full width of the diffraction peak, k represents constant (0.89) and θ refers to the diffraction angle.

3.3. Raman spectroscopy analysis

The ordered and disordered crystal lattice structure of the as-–synthesised nanocomposite was investigated using Raman spectroscopy (Fig. 3).

The peaks around 143, 232, 446, 515 and 612 cm^{-1} was obtained from the modes of E_g, E_g, B_{1g}, A_{1g} and E_g, which was found to match well with the anatase phase of TiO_2 [47]. The above observation confirmed that the anatase phase was dominant and correlated with the XRD results. The intense peak of E_g mode occurred because of the scattering from the (110) facet. The shifted E_g mode position was due to Gd modification from 637 to 643 cm^{-1}. The occurrence of the shift might be attributed to Gd_2O_3 E_g mode in the sample. The less intense peaks at 332 cm^{-1}, which occurred because of $A_{1g} + E_g$ symmetry vibrations of the cubic Gd_2O_3 confirmed the partial replacement of Ti by Gd in the TiO_2 lattice [48]. The narrow peaks, which were sharp and intense depicts the crystalline state of the nanocomposites confirmed that the crystallinity was not altered during the modification. The Raman spectra of GO sheets showed two distinct characteristic bands, D band (1366 cm^{-1}, which was the symmetric A_{1g} mode), and G band (1599 cm^{-1}, which was the E_{2g} mode of the sp^2 C atoms) [49]. This was consistent with earlier studies [50]. The nanocomposite spectra displayed peaks situated at 1315 and 1602 cm^{-1} and this comprised D and G bands of GO sheets, respectively [47]. The D band was attributed to the breathing mode of A_{1g} k–point photons. The G–band was obtained

from the centre zone of E_{2g} mode relating to the ordered sp^2–bonded C atoms. Hence, the degree of disorder in GO was obtained by the ratio of the intensity of D–band to that of the G–band [51]. Based on the different reduction levels, the intensity I_D/I_G ratio is a measure of defect concentration in graphene sheets, where a smaller intensity of I_D/I_G ratio signify fewer sp^3 defects/disorder and better average size of the in–plane graphitic crystallite sp^2 domains [52]. The I_D/I_G ratio (0.96) of GO sheets in this study was comparable with an earlier study (1.04) [53]. Moreover, TiO_2–GO and Gd–TiO_2–GO nanocomposites showed a slight decrease in the I_D/I_G ratio of 0.87 and 0.79, respectively, compared with GO sheets. This signifies a strong interaction between TiO_2 and GO sheets [54,55].

3.4. TEM and SEM analysis

The interior and superficial morphology of the as–synthesised pure TiO_2, TiO_2–GO and Gd–TiO_2–GO with a varying concentration of Gd was determined by TEM and SEM. The TEM image of TiO_2 nanoparticles showed a regular shape with even size distribution and well–distinct margins (Fig. 4a).

This proved that the method employed for the nanocomposite preparation was successful and this was ascribed to the enhancement of the sol–gel technique, which ensured the uniformity of Ti and O in the TiO_2 crystal structure. The TEM of GO nanosheets shown in Fig. 4b was observed to depict an irregular and wrinkled morphology. This was due to the affinity of the separate sheets to self–assemble, thereby forming multilayer aggregation of the individual sheets [56]. The prepared GO was found to be transparent, which established the two–dimensional nanosheets of GO [57]. The SEM image of Gd–TiO_2–GO showed agglomerated smaller crystallites (Fig. 4c). The TEM image of Gd–TiO_2–GO (Fig. 4d) revealed that Gd–TiO_2 nanoparticles, which served as support and electron donor were well–dispersed on GO sheets surface with a uniform size of 25–30 nm and thickness of 8–12 nm. This was much higher than pure TiO_2 (~20 nm), signifying a significant effect of Gd doping and GO sheets on the particle size of TiO_2 nanoparticles. The surface attachment of Gd–TiO_2 nanoparticles, rather than partial or complete wrapping by GO, guaranteed full contact of both Gd–TiO_2 nanoparticles and GO sheets, which could enhance the
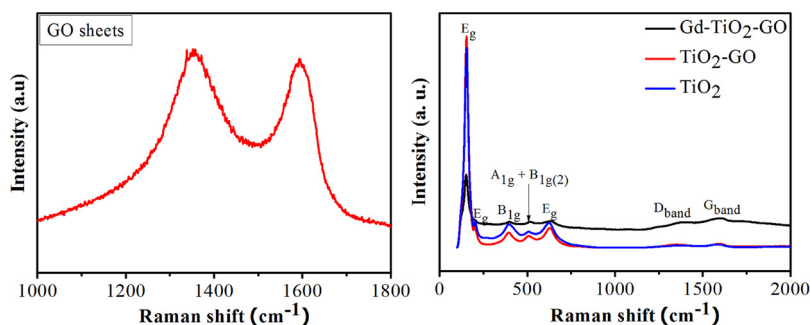

Fig. 3. Raman spectra of GO sheet, pure TiO_2, TiO_2–GO and Gd–TiO_2–GO nanocomposite.
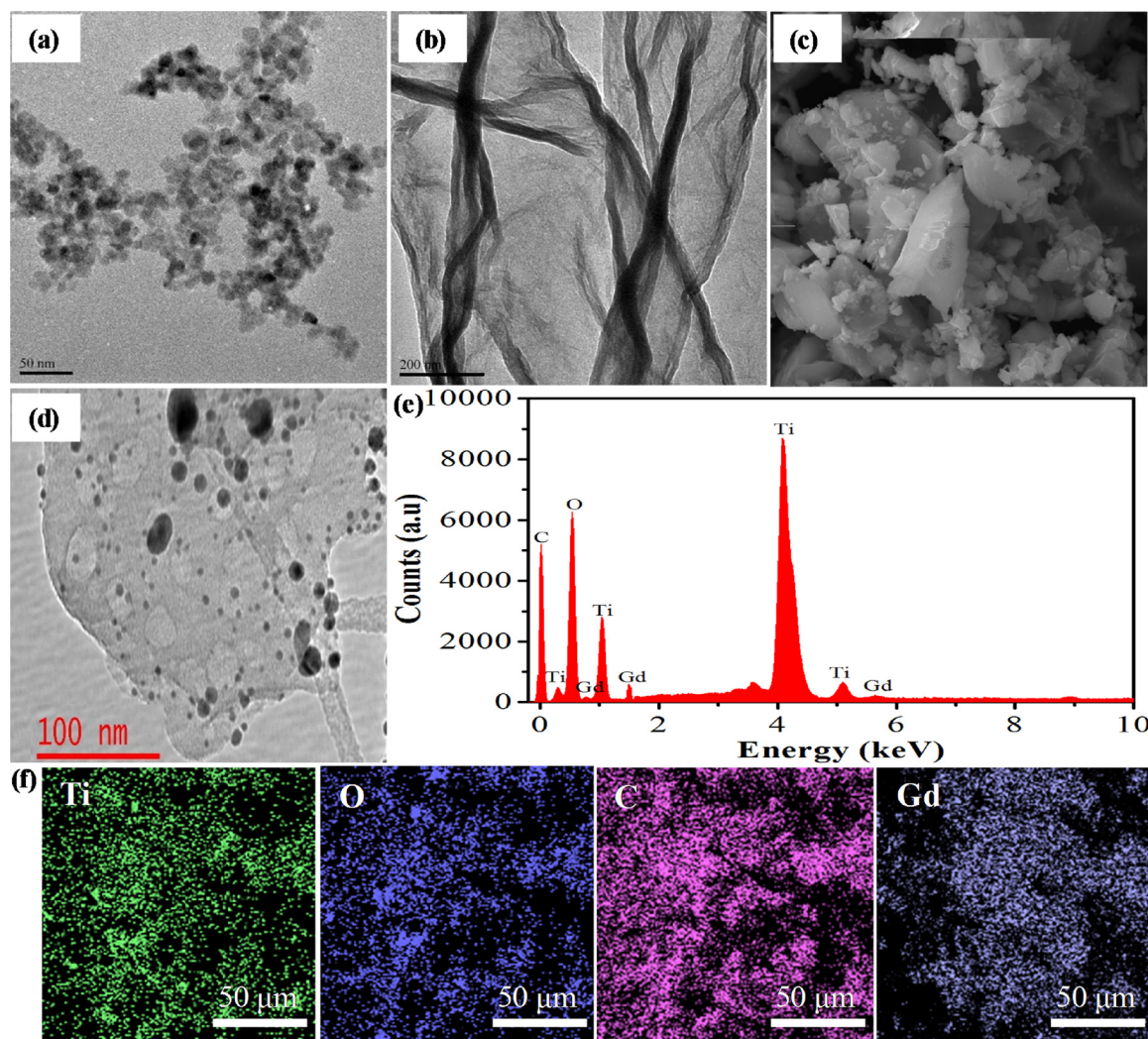
Fig. 4. TEM images of (a) TiO_2 and (b) GO sheets; (c) SEM image, (d) TEM image and (e) EDS of Gd–TiO_2–GO nanocomposite; (f) elemental mapping of Gd–TiO_2–GO nanocomposite.

photocatalytic performance. This confirmed the successful formation of GO layers around the Gd–TiO_2 nanoparticles. EDS study was carried out to confirm the elemental composition of Gd–TiO_2–GO nanocomposite (Fig. 4e). The EDS study confirmed the existence of Ti, O, C and Gd in the as–synthesised nanocomposites. The weight amount of Gd was 0.33, 0.66 and 1.10 wt% for the three different nominal compositions of Gd–TiO_2–GO nanocomposites, which was almost equal to the actual adding amount of Gd. The elemental mapping revealed the existence of Ti, O, C and Gd elements in Gd–TiO_2–GO nanocomposite (Fig. 4f) with an even distribution, signifies the existence of Gd and TiO_2–GO in the nanocomposites. The TEM, SEM, elemental mapping and EDS confirmed the successful fabrication of Gd–TiO_2–GO nanocomposites.

3.5. BET surface area analysis

The BET surface area analysis was carried out to offer the exact surface area of the prepared nanocomposites. Generally, a larger surface area of a semiconductor photocatalyst material induces a higher photoactivity and adsorbability. Therefore, nitrogen adsorption–desorption isotherm along with the Barrett–Joyner–Halenda approach was employed to study the influence of Gd doping and GO sheets on the BET surface area, pore size and volume of the as–prepared samples (Table 1).

The nitrogen adsorption–desorption isotherms provided in Fig. 5

Table 1
BET surface area, pore volume and size of the as–prepared photocatalysts.

Photocatalysts	BET Surface ($m^2 g^{-1}$)	Mean pore size (nm)	Pore volume ($cm^3 g^{-1}$)
TiO_2	82.56	24.56	0.06
TiO_2–GO	126.82	26.45	0.13
Gd–TiO_2–GO (0.3% Gd)	166.47	28.56	0.15
Gd–TiO_2–GO (0.6% Gd)	200.25	29.39	0.24
Gd–TiO_2–GO (1.0% Gd)	144.85	27.94	0.18

showed the type IV isotherm, which was characteristic of mesoporous material [58].

The BET surface area of pure TiO_2 was determined as 82.56 $m^2 g^{-1}$, which was much comparable to other studies [44]. The Gd–TiO_2–GO nanocomposites exhibited a wide pore size distribution (27.94–29.39 nm). The BET surface area of 200.25 $m^2 g^{-1}$ for Gd–TiO_2–GO (0.6% Gd) was *ca.* 1.20, 1.38, 1.58 and 2.23 times higher compared with Gd–TiO_2–GO (0.3% Gd) (166.47 $m^2 g^{-1}$), Gd–TiO_2–GO (1.0% Gd) (144.85 $m^2 g^{-1}$), TiO_2–GO (126.82 $m^2 g^{-1}$) and pure TiO_2 (82.56 $m^2 g^{-1}$). Therefore, Gd–TiO_2–GO (0.6% Gd) have the largest BET surface area, which was ascribed to its largest pore volume (0.24 $cm^3 g^{-1}$) compared with the other samples. Hence, the BET results revealed that increasing Gd content up to 0.6% in Gd–TiO_2–GO improved the surface area, which might expedite the photocatalysis of the
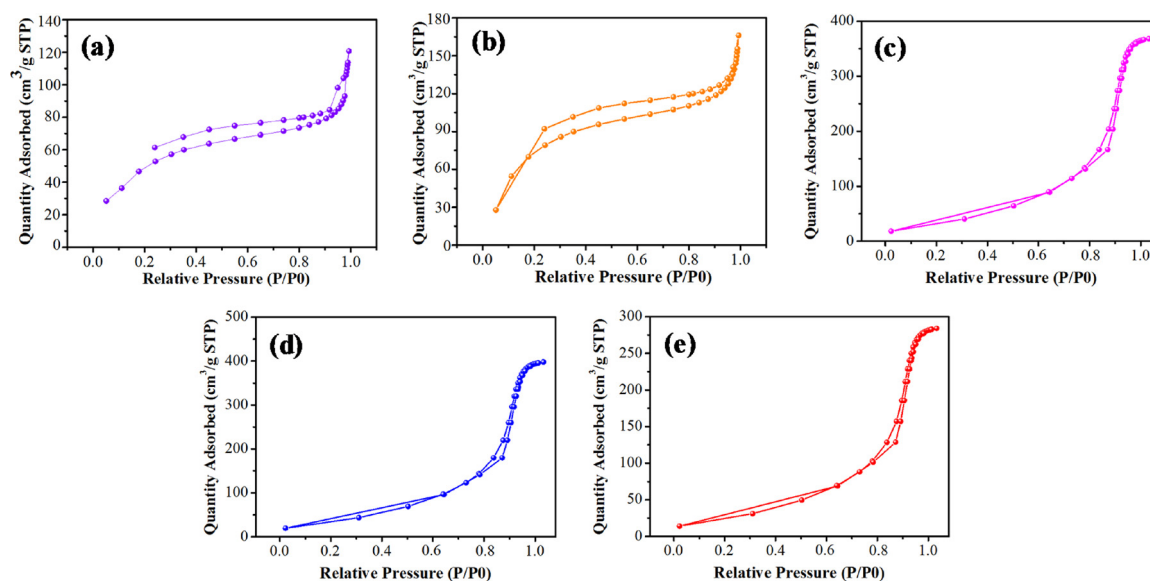
Fig. 5. Nitrogen adsorption–desorption of (a) pure TiO_2, (b) TiO_2–GO, (c) Gd–TiO_2–GO (0.3% Gd), (d) Gd–TiO_2–GO (0.6% Gd) and (e) Gd–TiO_2–GO (1.0% Gd) nanocomposites.

nanocomposite owing to the enhanced adsorbability.

3.6. X–ray photoelectron spectroscopy (XPS) analysis

The influence of GO sheets and Gd doping on the chemical binding environment and chemical composition of Gd–TiO_2–GO nanocomposite was further studied using XPS analysis. The surface chemical state of Ti, O and C in Gd–TiO_2–GO nanocomposite were studied using a high–resolution XPS and the results are given in Fig. 6.

The full–scale XPS pattern of Gd–TiO_2–GO revealed the presence of C, Ti and C (Fig. 6a). The binding energies of Ti 2p, O 1s and C 1s in the Gd–TiO_2–GO nanocomposite was located at 530.6, 458.9 and 284.3 eV, respectively. The binding energy peaks of Ti 2p core XPS was observed around 458.3 and 465.2 eV (Fig. 6b), which was due to the Ti $2p_{3/2}$ and Ti $2p_{1/2}$, respectively, consistent with other studies [59]. This was a

typical Ti(IV) sites bonded to oxygen atoms [60]. The Ti 2p peak, which was shifted to 0.6 eV indicated that the doped Gd^{3+} ions were occupied in the TiO_2 crystal structure [61]. The detailed chemical environment of the oxygen and carbon atoms was studied using a Gaussian fitting technique. An intense O 1s peak at 530.1 eV related to a typical Ti–O–Ti peak [62] (Fig. 6c). A broad and weak O 1s peak at 532.2 eV was related to the water molecules or −OH group on the Gd–TiO_2–GO nanocomposite surface [63]. The C 1s spectrum showed four main forms of C bonds located at 284.7, 284.9, 286.9 and 287.2 eV, which were related to C−C, C−OH, C−O (epoxy) and C=O groups, respectively [64].

3.7. Bandgap determination

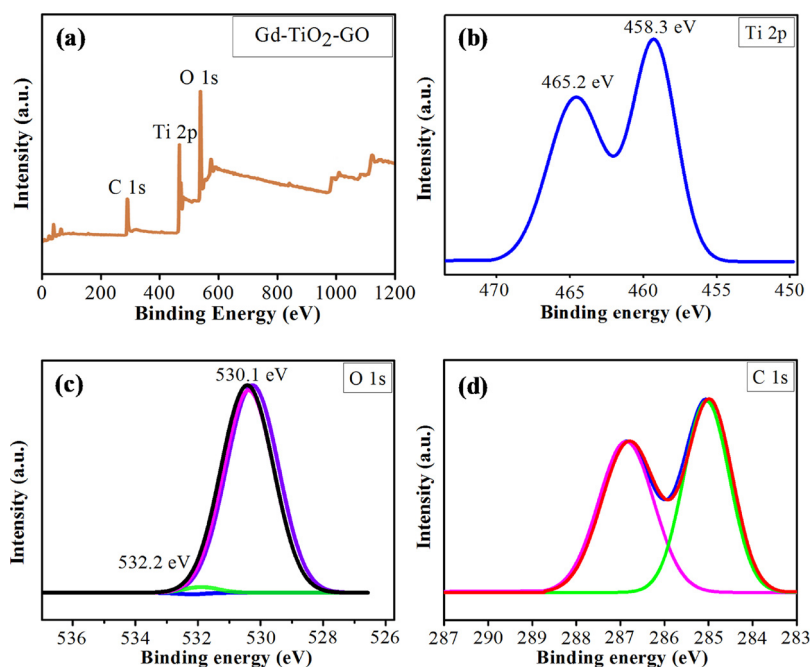The bandgap energy of the as–synthesised photocatalysts was

Fig. 6. The full–scale XPS pattern (a) and the individual high–resolution XPS spectra of (b) Ti 2p, (c) O1 s and (d) C 1 s of the Gd–TiO_2–GO nanocomposites.
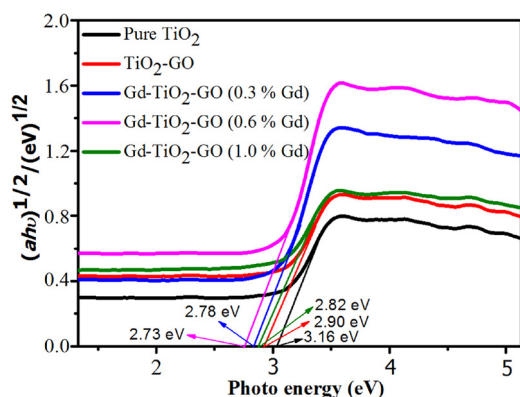
Fig. 7. The Kubelka–Munk plot of pure TiO_2, TiO_2–GO and Gd–TiO_2–GO nanocomposites with varied concentration of Gd.

evaluated from Tauc plots (Fig. 7) obtained from the Kubelka–Munk model, which was developed from the UV–vis diffuse reflectance.

These energy bandgaps were then obtained by extrapolating the linear fit to the photon energy axis. The bandgap measurement is related to Eq. (3):

$$(\alpha h\nu)1/r = h\nu \tag{3}$$

where α and r represent the absorption coefficient and the nature of transition, respectively [65]. r values of 1/2, 3/2, 2 and 3 represent direct allowed, forbidden, indirect allowed and indirect forbidden transitions, respectively. The bandgap energies were calculated as 3.16 eV for pure TiO_2 and 2.90, 2.78, 2.73 and 2.82 eV for TiO_2–GO, Gd–TiO_2–GO (0.3% Gd), Gd–TiO_2–GO (0.6% Gd) and Gd–TiO_2–GO (1.0% Gd) nanocomposites, respectively. The bandgap energies were found to decrease upon increasing the Gd concentration up to 0.6% and decreased further at 1.0%. This bandgap reduction was due to the decreases in descending shift of the Fermi energy level and free carrier concentration of Gd doping [66]. At high Gd concentrations, the bandgap increased because of the dominance of d–d transition over sp–d transition [67].

3.8. Optical analysis

Mostly, factors which can reduce the photoactivity of photocatalyst materials are the charge migration and separation, light irradiation absorption and absorption of organic pollutants [68]. Since the absorption ability of a photocatalyst plays a key influence on the photodegradation process, the optical property of the as–synthesised nanocomposites and pure TiO_2 were evaluated with UV–vis spectroscopy with the spectra shown in Fig. 8a and b.

The absorption edge of pure TiO_2 showed a blue shift because of its quantum confinement effect [69]. The TiO_2–GO nanostructure showed a red shift of the absorption edge and this was attributed to GO sheets in the nanocomposite, which eased the charge separation to reduce their

recombination rate. The photoactivity of the nanocomposite was observed to be extremely improved by loading Gd^{3+} ion onto the TiO_2–GO nanocomposite. Thus, the Gd doping narrows the energy bandgap and create a sub–bandgap in the TiO_2 to prolong the visible light absorption edge of the nanocomposite [70]. Again, Gd–TiO_2–GO (0.6% Gd) nanocomposite exhibited enhanced visible light response than TiO_2–GO, Gd–TiO_2–GO (0.3% Gd) and Gd–TiO_2–GO (1.0% Gd) nanocomposites, which was ascribed to the formation a sub–bandgap energy state within the TiO_2 nanoparticle by the Gd^{3+} ion. This occurrence allows the excitation of electrons from the TiO_2 valence band (VB) into the created intermediate states [71]. Additionally, the incorporation of GO improved the visible light absorption of the nanocomposite compared with pure TiO_2. This occurrence might be attributed to the fact that GO sheets create a sub–bandgap energy inside TiO_2 crystal structure permitting the transfer of electrons from the intermediary states to the conduction band (CB) of TiO_2 [72]. Besides, GO behave as photosensitisers and therefore absorb visible light and excite electrons to the CB [73]. This enhancement originates from the mutual effect of Gd^{3+} ion and GO.

3.9. Computational study

3.9.1. Catalytic stability

To construct the theoretical model of TiO_2–GO and Gd–TiO_2–GO nanocomposites, the geometric structures of GO sheets and pure TiO_2 was initially studied. The nanocomposite was composed of 4×2 and 4×4 supercells for GO sheets and pure TiO_2, respectively, with a lattice mismatch of 2.99%. Such a small lattice mismatch confirmed the experimental realisation of TiO_2–GO and Gd–TiO_2–GO nanocomposites [74]. The lattice parameters of anatase TiO_2 were calculated as $a = b = 3.796$ Å, $c = 9.947$ Å and $\alpha = \beta = \gamma = 90°$ after full geometry optimisation. The Ti−O had a bond length of 1.950 Å, which was comparable with earlier studies [75]. Moreover, the bonding length of Gd–O (2.211 Å) was higher than Ti–O. This was attributed to the larger atomic radius of Gd^{3+} (0.938 Å) than that of Ti^{4+} (0.605 Å) [76].

Since the interaction between GO and TiO_2 determined the photocatalytic stability and activity, the separation and geometries of as–prepared nanocomposites were investigated. The interfacial interaction in the nanocomposites could be properly assessed using the equilibrium distance (interfacial separation) between the individual components of the nanocomposites. Generally, stronger interaction correlates with smaller interfacial separation [77]. For the TiO_2–GO nanocomposite, the interfacial separation between the bottom of the TiO_2 slab surface and GO sheets was measured as 3.34 Å, while the interlayer spacing in Gd–TiO_2–GO composite was 3.05 Å. These were consistent with those in other GO–based nanocomposites [78,79]. This showed that the interfacial interactions were stronger in the Gd–TiO_2–GO nanocomposite than TiO_2–GO nanocomposite. Hence, the Gd–TiO_2–GO nanocomposite might have a higher stability than the TiO_2–GO nanocomposite. After geometry optimisation, the shapes of GO and TiO_2 monolayers showed little change, suggesting weak vdWs interaction.
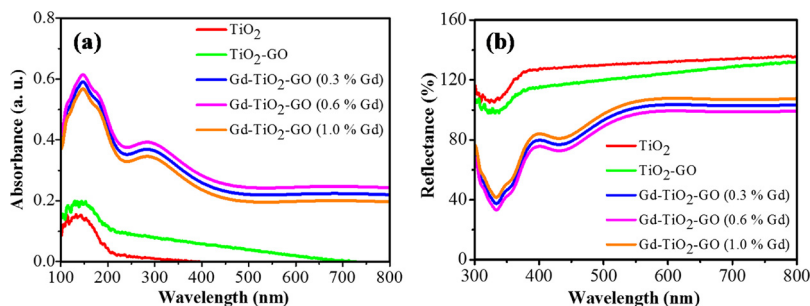

Fig. 8. (a) UV–vis spectra and (b) diffuse reflectance spectra of pure TiO_2 nanoparticles, TiO_2–GO and Gd–TiO_2–GO nanocomposites with varied concentrations of Gd.

The catalytic stability of TiO$_2$–GO and Gd–TiO$_2$–GO nanocomposites was evaluated using the interface adhesion energy shown in Eqs. (4) and (5), respectively:

$$E_{ad} = [E_{\text{TiO}_2-\text{GO}} - E_{\text{TiO}_2} - E_{\text{GO}}]/S \tag{4}$$

$$E_{ad} = [E_{Gd-\text{TiO}_2-\text{GO}} - E_{\text{TiO}_2} - E_{GO} - \mu_{\text{Gd}} + \mu_{\text{Ti}}]/S \tag{5}$$

where $E_{\text{TiO}_2-\text{GO}}$, E_{TiO_2}, E_{GO} and $E_{Gd-\text{TiO}_2-\text{GO}}$ are the total energies of TiO$_2$–GO, TiO$_2$, GO and Gd–TiO$_2$–GO nanocomposite, respectively. μ_{Ti} and μ_{Gd} are the respective chemical potential of the host Nb ion and V dopant. S is the interface area in the plane. At the equilibrium conditions, TiO$_2$ must satisfy the following equation:

$$\mu_{\text{Ti}} + 2\mu_{\text{O}} = \mu_{\text{TiO}_2} \tag{6}$$

however, in the thermal equilibrium condition,

$$\mu_{\text{TiO}_2} = E_{\text{TiO}_2} \tag{7}$$

$$E_{\text{TiO}_2} = \mu_{\text{Ti}} + 2\mu_{\text{O}} + \Delta H_f(\text{TiO}_2) \tag{8}$$

where E_{TiO_2} is the total energy of TiO$_2$. μ_{Ti} chemical potential was obtained from the formation energy of Ti atom in pure TiO$_2$. However, μ_{O} was obtained as half the energy of the oxygen molecule [80]. For the Gd dopant, μ_{Gd} was calculated from the pure Gd ($\mu_{\text{Gd}} = \mu_{Gd}^{metal}$) [80]. $\Delta H_f(\text{TiO}_2)$ is the formation energy of pure TiO$_2$.

Hence, under thermal equilibrium condition, $\Delta H_f(\text{TiO}_2)$ was obtained as:

$$\Delta H_f(\text{TiO}_2) = \Delta\mu_{\text{Ti}} + \Delta 2\mu_{\text{O}} \tag{9}$$

where, $\Delta\mu_{\text{O}} = \mu_{\text{O}} - E_{\text{O}}$, was the same as that of Ti. To maintain thermodynamic equilibrium of the crystalline phase, the chemical potential of each elements cannot surpass that of the corresponding gaseous (O) or pure (Ti) state [81], *i.e.*

$$\Delta\mu_{\text{Ti}} < 0, \Delta\mu_{\text{O}} < 0 \tag{10}$$

The calculated chemical potentials were calculated as –4.41, −8.90 and –7.92 eV for O, Ti and Gd atoms, respectively. The interface adhesion energies were calculated as –2.42 and –3.07 eV Å^{-2} for TiO$_2$–GO and Gd–TiO$_2$–GO nanocomposites, respectively. Thus, the negative interface adhesion energy further confirmed the observed experimentally fabricated nanocomposites. Moreover, the interface adhesion energy of TiO$_2$–GO nanocomposite was less negative than Gd–TiO$_2$–GO nanocomposite, and this indicated superior stability and strong interaction between the GO and Gd–TiO$_2$–GO monolayers.

3.9.2. Band structure and density of states

To evaluate the effect of interfacial interactions, it is insightful to analyse the band structures and projected density of states (PDOS) of GO and TiO$_2$ before and after the formation of the nanocomposites were evaluated. The band structures, as well as the corresponding bandgap energies of the TiO$_2$ and GO, are presented in Fig. 9a and b, respectively.

For pure TiO$_2$, the valence band maximum (VBM) and conduction band minimum (CBM) was situated at the X and Γ points, respectively with an indirect bandgap value of 3.27 eV. This was slightly higher than the experimental value (3.16 eV). Clearly, the PDOS along the energy level agreed well with the electronic band structure, indicating that the result was reliable. Moreover, the PDOS of pure TiO$_2$ was presented to show the contributions in the VBM and CBM. For pure TiO$_2$, the VBM was mostly dominated by O 2p state, whereas the CBM comprised Ti 3d state with hybridisation from O 2p and Ti 4s states (Fig. 9a). The PDOS results of pure TiO$_2$ was consistent with other theoretical studies [82]. Fig. 9b showed that the GO sheet was an indirect bandgap semiconductor with the VBM and CBM positioned at the T and Γ points simultaneously and the E_g was 2.75 eV, which was within the bandgap range of 2.4–4.3 eV [83]. In addition, as shown in Fig. 9b, the states in the CBM comprised C 2p and 2 s states, while the VBM was primary

consisted of O 2p and O 2 s states. Unlike pure TiO$_2$, both the CBM and VBM of TiO$_2$–GO nanocomposite were simultaneously located at the YΓ points. Therefore, TiO$_2$–GO nanocomposite showed a direct bandgap of 2.84 eV. Obviously, for the TiO$_2$–GO nanocomposite, the CBM composed of the states of the GO sheets (explicitly, C 2p, O 2p and O 2 s states), while the VBM comprised orbitals from the TiO$_2$ (largely Ti 3d state). Moreover, the Gd–TiO$_2$–GO nanocomposite was a direct bandgap semiconductor with both the VBM and CBM positioned simultaneously at the *AB* points with a value of 2.78 eV (Fig. 9d). Due to the weak quantum size effects and interaction between GO and TiO$_2$, the bandgaps of TiO$_2$–GO and Gd–TiO$_2$–GO nanocomposites were reduced compared to pure TiO$_2$. This makes the charge migration from the VB to the CB of the nanocomposites easier. Compared to the Gd–TiO$_2$–GO nanocomposite, the VB contained Ti 3d and O 2p states of TiO$_2$ together with Gd 6 s state. However, C 2p state dominated the CBM with contribution from Gd 5d and O 2 s states. From Fig. 9d, TiO$_2$ dominated the VBM of Gd–TiO$_2$–GO nanocomposite, while the CBM was from GO sheets with some contribution from Gd^{3+} ion for both CBM and VBM. Therefore, a type–II band alignment occurred between the GO and TiO$_2$, with the TiO$_2$ having a higher electron affinity of 5.16 eV compared with GO sheets (4.95 eV). Moreover, our calculated electron affinity agreed with those theoretically calculated for anatase (5.10 eV) [84].

To further explore the origin of charge transfer, the charge density for the lowest unoccupied levels (LUL) and highest occupied levels (HOL) was plotted, as given in Fig. 10. Clearly, the VBM and CBM were localised in a different sheet and this signified different spatial distributions of charge carriers. For the TiO$_2$–GO nanocomposite, the LUL was localised around the GO sheet, whereas the HOL consisted of orbitals from TiO$_2$.

However, for Gd–TiO$_2$–GO nanocomposite, the introduction of Gd^{3+} ion led to electrons and holes enrichment around the Gd atom. This showed that the Gd atom could accept electrons from the TiO$_2$ surface and donate it to GO sheets.

3.9.3. Charge transfer and mechanism analysis

The electronic band structure variation of TiO$_2$–GO and Gd–TiO$_2$–GO nanocomposites signifies a much charge transfer between the individual monolayers of the nanocomposites. To visualise the interfacial charge migration, the charge density difference was calculated, see Fig. 11.

The purple and green regions are the charge density accumulation and depletion, respectively. The charge density redistribution mostly observed around the TiO$_2$–GO interface region, but less charge density was found in the inner TiO$_2$ (Fig. 11a). This was ascribed to weak vdWs interactions between GO sheets and TiO$_2$. Nonetheless, for the Gd–TiO$_2$–GO nanocomposite (Fig. 11b), a stronger charge density was observed at the interface region and several atoms in the GO sheets due to the relatively shorter interface distance. The change of interfacial charge density of the Gd–TiO$_2$–GO nanocomposite showed that the electrons mostly migrated from TiO$_2$ to GO sheets *via* the Gd^{3+} ion at the interface, while the holes left on the TiO$_2$ side. A further Bader Mulliken charge population analysis revealed a total charge transfer of 0.23 and 0.86 |e| for the TiO$_2$–GO and Gd–TiO$_2$–GO nanocomposites, respectively. This implied that the number of electrons transferred at the interface of Gd–TiO$_2$–GO was more than that transferred to the TiO$_2$–GO interface. The more charge migration further confirmed the stronger interfacial interactions in the Gd–TiO$_2$–GO nanocomposite compared with the TiO$_2$–GO nanocomposite.

To explain the origin of interfacial charge migration, work function ($\Delta\Phi$), which is the least energy needed to remove an electron from a solid to a surface was calculated. Work function is an essential electronic property of semiconductor photocatalyst, which offers a better insight into the relative position of the Fermi energy levels [85]. The calculated work functions were 4.73 and 5.39 eV for TiO$_2$ and GO monolayers, respectively (Fig. 12a and b).
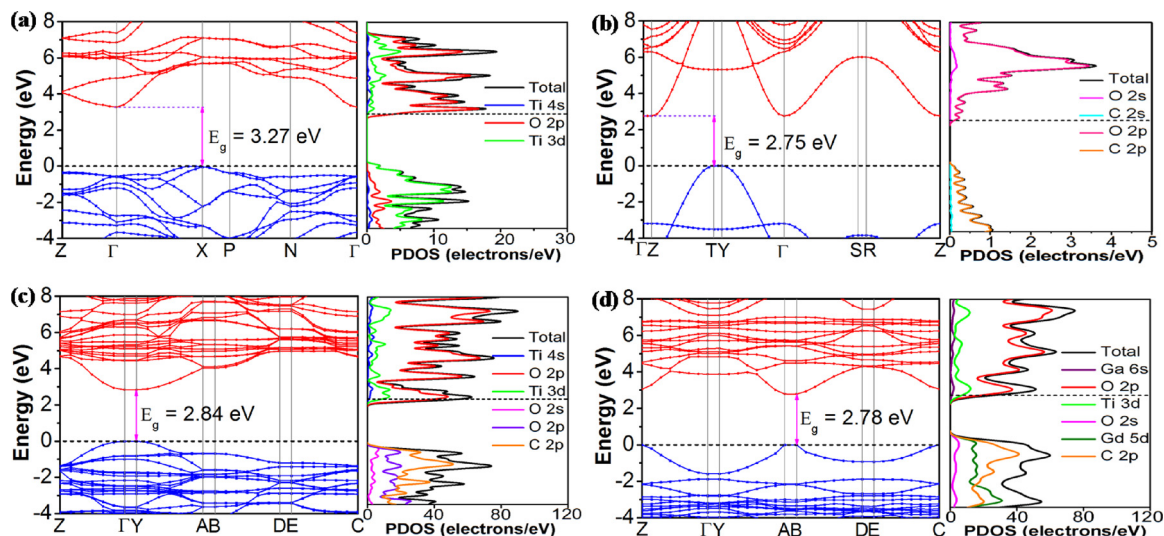
Fig. 9. The calculated band structure and PDOS of (a) pure TiO_2, (b) GO sheets, (c) TiO_2–GO and (d) Gd–TiO_2–GO nanocomposites.

The work function of anatase TiO_2 was slightly lower than the work function range of 4.90 eV previously reported [86]. Moreover, work function of GO sheet was within the calculated work function range of 4.43 to 5.72 eV [85]. When the GO sheets were loaded onto TiO_2 or Gd–doped TiO_2 by weak van der Waals interaction, the work function of TiO_2–GO and Gd–TiO_2–GO nanocomposites were about 4.49 and 4.20 eV (Fig. 12c and d), respectively, and this was smaller than that of the TiO_2 monolayers. The reduced work function in the nanocomposites confirmed the higher charge migration. The change in work function of Gd–TiO_2–GO ($\Delta\Phi$ = 0.53 eV) was higher compared with the TiO_2–GO ($\Delta\Phi$ = 0.24 eV). The high work function shift in the Gd–TiO_2–GO photocatalyst showed that the occupancy of GO sheets orbitals was effective below the CB of Gd–TiO_2–GO nanocomposites and hence

lowers the bandgap energy [75]. The work function of TiO_2 was smaller than that of GO sheet. These phenomena indicated that the transferred of electrons from TiO_2 to GO sheet surface was thermodynamically favoured when GO sheets were attached to TiO_2. Subsequently, such charge migration between TiO_2 and GO sheets induced built–in internal electric field directed from TiO_2 to GO sheet, which might decrease the recombination rate, which was vital to the separation of charge carriers and photocatalytic performance.

Besides the visible light absorption and suitable band gap, smaller effective mass is another important factor for realising a higher photoactivity. Therefore, it is interesting to know whether visible light absorption edge and suitable bandgap can affect the carrier mobility of the as–prepared nanocomposites. The effective mass of holes (m_h^*) and
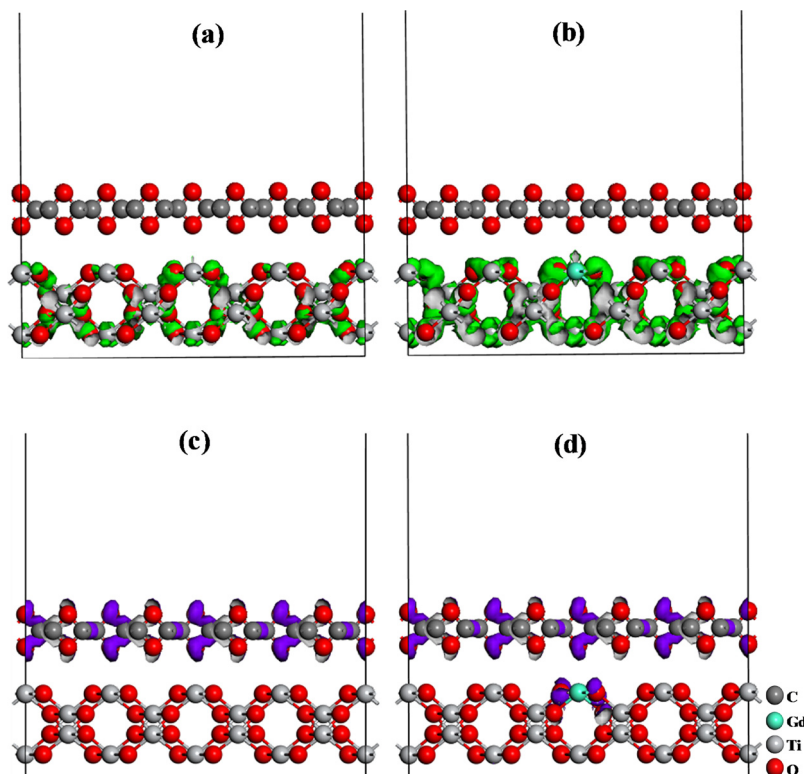

Fig. 10. The charge density distributions of the HOL (a, b) and LUL (c, d) with an isovalue of 0.05 e Å^{-3} for the TiO_2–GO and Gd–TiO_2–GO nanocomposites.
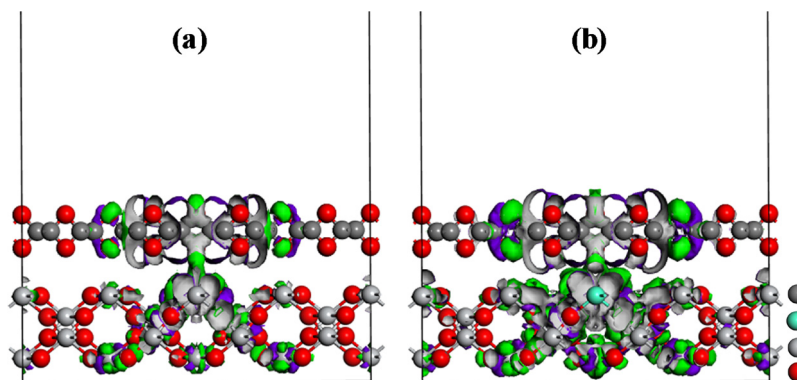
Fig. 11. The charge density difference of (a) TiO$_2$–GO and (b) Gd–TiO$_2$–GO nanocomposites. (For interpretation of the references to colour in the text, the reader is referred to the web version of this article.)

electrons (m_e^*) were accessed by fitting parabolic function to the VBM and CBM, following Eq. (11) [87]:

$$m^* = \hbar^2 \left(\frac{d^2E}{dk^2}\right)^{-1}, \tag{11}$$

where m^*, $\hbar$, $\frac{d^2E}{dk^2}$ and E are the effective mass, reduced Planck constant, second order coefficient term and band edge energy as a function of wave vector k, respectively [88]. Comparing the effective mass, the effective masses of electron (hole) values of both TiO$_2$–GO (1.06 (0.99) m_o) and Gd–TiO$_2$–GO (0.63 (0.86) m_o) nanocomposites were smaller than those of TiO$_2$ (1.87 (1.23) m_o). Generally, materials with a smaller effective mass can easily transfer electron–hole pairs to the reactive sites during the photocatalytic reactions. Therefore, Gd–TiO$_2$–GO nanocomposites exhibited an enhanced separation and small possibility of recombination rate of charge carriers.

3.10. Photocatalytic analysis

A further photocatalysis experiment, such as photodegradation of IC dye was performed based on the characterisation of Gd–TiO$_2$–GO nanocomposite. The photoactivity of the as–synthesised nanocomposites were assessed for the photodegradation of IC dye under UV irradiation. The concentration of IC dye was proportional to the absorbance based on the Beer–Lambert Law [89]:

$$A = \varepsilon Cl \tag{12}$$

where A, ε, C and l are the absorbance, molar absorbing coefficient, concentration of absorbing components and length of absorbing layers, respectively. Fig. 8a shows the process of photodegradation using the UV–vis change of IC dye relative to the irradiation time for degradation of Gd–TiO$_2$–GO nanocomposite.

It was observed that within 0–210 min over a wavelength range of 450–700 nm, a maximum absorption peak of 610 nm of IC dye begin to decrease with increasing exposure time, signifying the IC dye was being degraded by the nanocomposite. Thus, the absorbance was gradually decreased with increasing visible irradiation time.

3.11. Photoelectric properties

Generally, an IC photodegradation process comprises charge carrier separation, migration and recombination where the photogenerated recombination rate of charge carriers is one of the key roles mostly responsible for the low photoactivity. Doping often controls the charge carrier separation at the crystal structure of the host semiconductor [90]. Graphene–derivatives is a suitable material owing to its 2D π–conjugation structure [91], and has been effectively applied to TiO$_2$ with reduced recombination rate of charge carriers [92]. Therefore, to further evaluate the influence of GO sheets and Gd doping on TiO$_2$, the charge recombination nature was studied via photoluminescence (PL) spectra (Fig. 13b) with an excitation λ of 320 nm and this was where it can only excite electrons in TiO$_2$ into the excited state [93]. The PL spectra have shown to reveal the efficiency of charge transfer and recombination rate of photocatalyst [94], as well as offering more
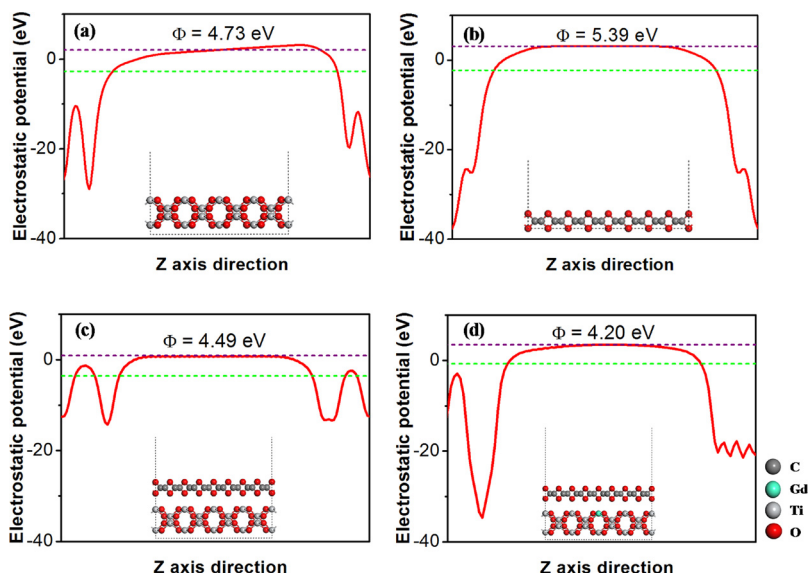

Fig. 12. The calculated work function of (a) TiO$_2$, (b) GO sheet, (c) TiO$_2$–GO and (d) Gd–TiO$_2$–GO nanocomposites. The purple and green dashed lines are the vacuum and Fermi energy levels, respectively. (For interpretation of the references to colour in this figure legend, the reader is referred to the web version of this article.)
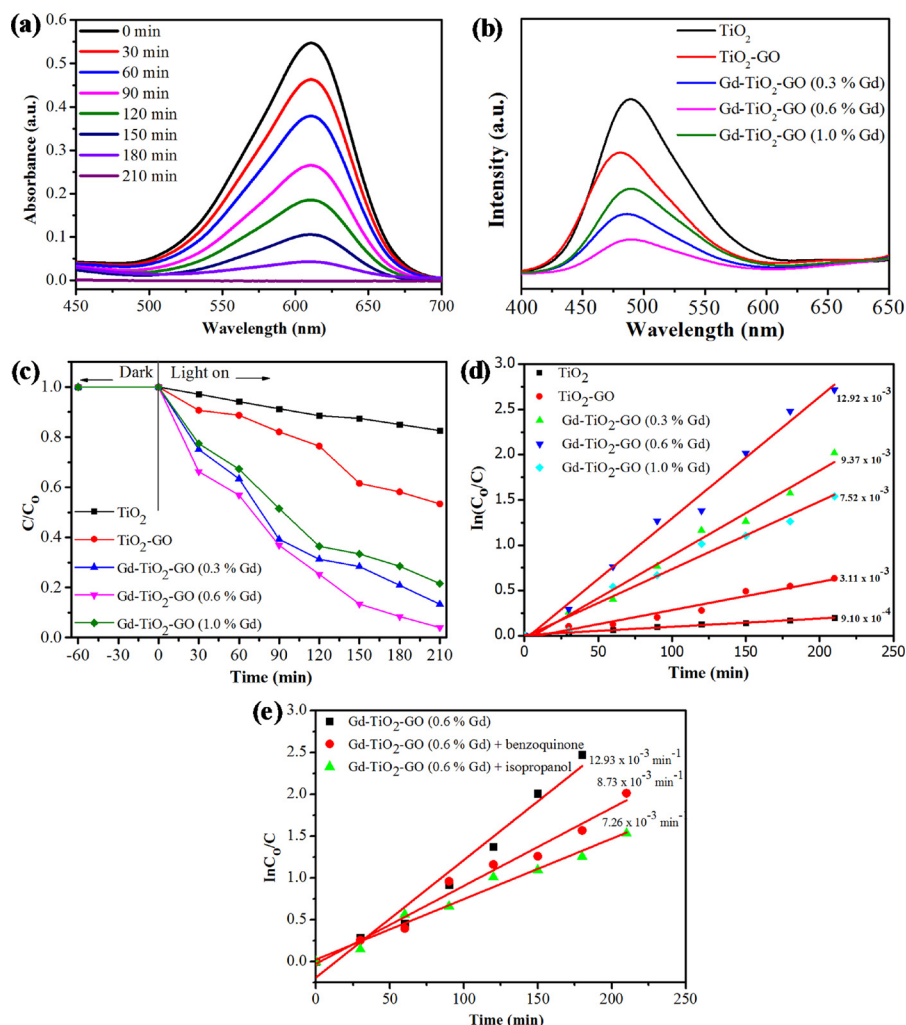
Fig. 13. (a) IC dye photodegradation profile against the irradiation time of Gd–TiO₂–GO (0.6% Gd) nanocomposite, (b) photoluminescence spectra of the as–prepared samples, (c) IC dye degradation profile in the dark and light on of the as–prepared samples, (d) kinetics of IC photodegradation for the first 210 min of the as–prepared samples and (e) photodegradation rate of IC dye in the presence of radical scavengers.

Table 2
The measured bandgap energy and percentage degradation of IC dye under simulated light irradiation.

Sample	Bandgap (eV)	Degradation (%)	K (min⁻¹)	R^2
TiO₂	3.16	19	9.10×10^{-4}	0.9975
TiO₂–GO	2.90	48	3.11×10^{-3}	0.9828
Gd–TiO₂–GO (0.3% Gd)	2.78	65	9.37×10^{-3}	0.9922
Gd–TiO₂–GO (0.6% Gd)	2.73	97	12.92×10^{-3}	0.9806
Gd–TiO₂–GO (1.0% Gd)	2.82	50	7.52×10^{-3}	0.9933

insights into the kinetics of photodegradation [95]. Normally, the lower the intensity of the PL emission spectrum, the less recombination of charge carriers and the higher the photoactivity of semiconductor photocatalysts [96]. The PL spectra were similar to other studies [97]. Obviously, the emission intensity of PL spectra for Gd–TiO₂–GO was lower compared with TiO₂–GO and TiO₂. Thus, the lower PL intensity for Gd–TiO₂–GO revealed that the Gd³⁺ ion and GO sheets intensely reduce the charge carrier recombination rate occurring on the TiO₂ surface, thereby enhancing their separation. Thus, in Gd–TiO₂–GO nanocomposite, GO act as an electrical pathway for the photogenerated electrons in TiO₂, whereas Gd³⁺ ion might act as an electron acceptor

during the photodegradation process. The Gd–TiO₂–GO (0.6% Gd) nanocomposite with lowest PL intensity, demonstrated the highest efficiency of charge carrier separation and enhanced adsorption of IC dye. Thus, the Gd–TiO₂–GO (0.6% Gd) nanocomposite should successfully reduce electrons recombination with holes during the charge carrier migration process with more charges to form reactive species to expedite the photodegradation of IC dye.

3.12. Kinetic studies

To examine the self–photosensitisation effect of IC dye in the photodegradation process, a blank experiment without semiconductor photocatalyst in the dark was also carried out and the plot is as given in Fig. 13c. No apparent IC dye photodegradation was observed without semiconductor photocatalyst, signifies that the self–photosensitisation influence of IC dye could be ignored in this study. Table 2 showed that the percentage degradation of the nanocomposites of which Gd–TiO₂–GO (0.6% Gd) nanocomposite degrade the IC dye by 97%, while the pure TiO₂ nanoparticle degraded the IC dye by 19%.

The degradation efficiency of up to 97% is achieved by Gd–TiO₂–GO (0.6% Gd) after 210 min irradiation. Nevertheless, when the Gd concentration was further increased above its optimum concentration, the photodegradation activity was reduced. This was because a large amount of Gd³⁺ ion can absorb some light, while some Gd³⁺ ion may serve as a recombination centre rather than providing an electron

transfer pathway. Thus, in this study, 0.6% Gd was the most suitable concentration for TiO2–GO photocatalyst. Therefore, Gd–TiO2–GO (0.6% Gd), based on its excellent photocatalytic activity, was selected as the final photocatalyst to investigate the in–situ trapping experiments. The high photodegradation performance of Gd–TiO2–GO (0.6% Gd) was ascribed to the easy separation of charge carriers, the reduction of the bandgap energy by Gd doping, which caused the enhancement of visible light absorption edge, the ease at which the IC dye was adsorbed on the photocatalyst surface owing to the π–π interactions found in both GO and IC molecules and the use of optimum amount of Gd, which promoted the scavenging of electrons inside the CB thereby restricting their recombination with the holes to improve the photodegradation activity of the nanocomposite.

Fig. 13d shows the IC photodegradation rate as a function of irradiation time for pure TiO2, TiO2–GO and the various Gd loaded TiO2–GO photocatalysts. Based on earlier studies [98], the photodegradation of dye molecules could correspond to a pseudo first–order reaction kinetics via the Langmuir–Hinshelwood model, which is well–known for the photodegradation of several dye molecules using a semiconductor photocatalyst. The Langmuir–Hinshelwood model was employed to fit the experimental data, and it can be mathematically expressed according to Eq. (13):

$$\ln(C/C_0) = kt \tag{13}$$

where t is irradiation time and k is photodegradation rate constant, which was evaluated from a linear fit to the experimental data, as given in Fig. 13d. The degradation was quantitatively determined by comparing the photodegradation reaction rate constants, which was evaluated from the plot of $\ln(C_0/C)$ vs. irradiation time. All the curves were nearly linear, revealing that IC dye degradation conforms to the pseudo–first–order kinetics. The photodegradation rate in Table 2 revealed that Gd–TiO2–GO (0.6% Gd) was 14.19–fold, 4.15–fold, 1.37–fold and 1.72–fold higher compared to the pure TiO2, TiO2–GO, Gd–TiO2–GO (0.3% Gd) and Gd–TiO2–GO (1.0% Gd), respectively, signifying that Gd–TiO2–GO (0.6% Gd) showed higher photocatalytic efficiency. The superior activity of Gd–TiO2–GO (0.6% Gd), might be largely ascribed to the effective charge migration from TiO2 to GO via Gd^{3+} ion.

3.13. Experiments for radical scavengers

To comprehend the photocatalytic reaction mechanisms, the main reactive species involved in the photodegradation process were evaluated using reactive species trapping experiments. In this study, about 10 mL of benzoquinone (BQ), which is a scavenger for $O_2^{-\cdot}$ radicals and 10 mL of isopropanol (IPA), which is a scavenger for $HO^{\cdot}$ radicals were added to the IC dye solution having Gd–TiO2–GO (0.6% Gd) nanocomposite. The photoactivity of Gd–TiO2–GO (0.6% Gd) photocatalyst for the degradation of IC dye in the existence of scavengers is shown in Fig. 13e. The presence of IPA ($HO^{\cdot}$ scavenger) in the IC dye solution led to the rapid deactivation of Gd–TiO2–GO (0.6% Gd) for the photodegradation of IC dye. Moreover, the effectiveness of the photodegradation of IC dye was reduced substantially when BQ ($O_2^{-\cdot}$ scavenger) was added compared to IPA. In the presence of BQ, the degree of photodegradation of IC dye by the photocatalyst decrease to 8.72×10^{-3} during the photocatalysis process, which was slower than that without BQ (12.92×10^{-3}). This corresponded to a maximum photodegradation of 77% and a decrease of 20% compared to the absence of BQ (97%), as presented in Table 3.

Moreover, adding iso–propanol reduced the rate of photodegradation to 7.17×10^{-3} and this was about 1.8–fold slower compared with the absence of iso–propanol. The lower degradation efficiency obtained was due to the presence of radical scavengers, which consume some of the active species with only a few lefts for the IC dye degradation, thereby lowering the degradation efficiency. The obtained degradation of 69% decrease to 28% when IPA was present. The results obtained suggest that both $O_2^{-\cdot}$ and $HO^{\cdot}$ radicals were actively involved in the

Table 3
The rate of photodegradation in the presence or absence of radical scavengers.

Nanocomposite	Photodegradation (%)		k (min^{1})	R^2
	Scavengers	No scavengers		
Gd–TiO2–GO (0.6% Gd)		97	12.92×10^{-3}	0.9921
Gd–TiO2–GO (0.6% Gd) + BQ	20	77	8.72×10^{-3}	0.9906
Gd–TiO2–GO (0.6% Gd) + IPA	28	69	7.17×10^{-3}	0.9842

photodegradation of IC dye. This study, therefore, confirmed that the presence of both $O_2^{-\cdot}$ and $HO^{\cdot}$ radicals brought about the IC dye degradation [99].

3.14. Total organic carbon (TOC) analysis

Fusion UV/persulfate TOC analyser was employed to investigate the photodegradation of IC dye using Gd–TiO2–GO (0.6% Gd) nanocomposite. This nanocomposite was used for the TOC studies since it showed the most improved visible light photoactivity and degradation efficiency. The result of the TOC analysis, which was carried out using varied intervals of time up to 5 h (Fig. 14a), showed that about 85% TOC removal was achieved, suggesting that an appreciable degree of complete mineralisation has been achieved.

The results again showed that the nanocomposite (Gd–TiO2–GO (0.6% Gd)) was responsible for the whole mineralisation of the IC dye to less toxic compounds. Besides the photoactivity, the stability and reusability of any photocatalyst is significance to industrial application and practical utility. The stability of Gd–TiO2–GO (0.6% Gd) nanocomposite was carried out through recycling. Five (5) runs of recycling IC dye photodegradation experiment was performed in this study. Deionised water and ethanol were employed for washing after which it was dried before reused again. Fig. 14b showed that about 87% maximum IC dye removal by the nanocomposite was recorded and the reduced IC dye degradation efficiency was due to the weight loss of collection of TiO2, which was beneficial for the separation and reuse of Gd–TiO2–GO (0.6% Gd) photocatalyst [100] and partial occupation of the active sites by carbon deposits formed on the photocatalyst surface during the photodegradation of IC dyes [44]. Therefore, the photoactivity of Gd–TiO2–GO (0.6% Gd) retains a high level of performance during the cycling photodegradation of IC dye, suggesting a better reusability and stability of Gd–TiO2–GO (0.6% Gd).

3.15. Mott–Schottky plot analysis

The effects of Gd doping on the flat–band potential (E_{fb}) of TiO2–GO nanocomposite was studied using Mott–Schottky plots. Normally, the accumulation of electrons certainly induces a Fermi energy level shift [101]. The E_{fb} of the as–fabricated samples was evaluated using the Mott–Schottky equation [102]:

$$\frac{1}{C^2} = \frac{2}{e\varepsilon\varepsilon_0 N_D}\left(E - E_{fb} - \frac{k_B T}{e}\right) \tag{14}$$

where C, ε, ε_0, N_D, E, E_{fb}, k_B, T and e are the space charge capacitance, dielectric constant, permittivity of free space, electron carrier density, external applied potential, flat band potential, Boltzmann constant, temperature and elemental charge of the photocatalyst, respectively. The Mott–Schottky results are shown in Fig. 15.

The value of E_{fb} was calculated by taking the x–intercept of a linear fit to Mott–Schottky plot against the applied potential. All the samples gave a negative E_{fb} value and this indicated that the as–prepared samples showed a p–type semiconductor property. The E_{fb} of pure TiO2, TiO2–GO, Gd–TiO2–GO (0.3% Gd), Gd–TiO2–GO (0.6% Gd) and Gd–TiO2–GO (1.0% Gd) were ca. –0.48, –0.43, –0.36, –0.34 and –0.38 V
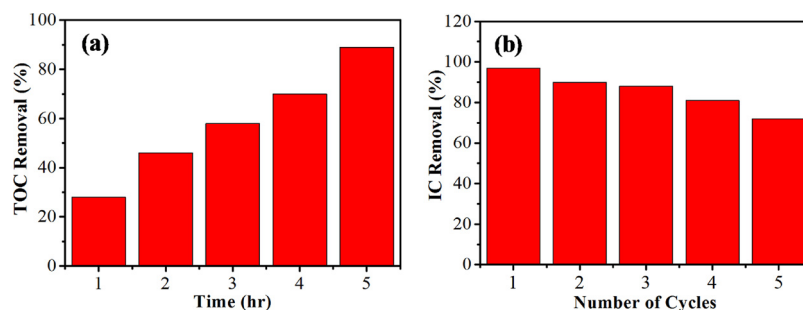
Fig. 14. (a) TOC removal and (b) recyclability studies of Gd–TiO$_2$–GO (0.6% Gd) nanocomposite.
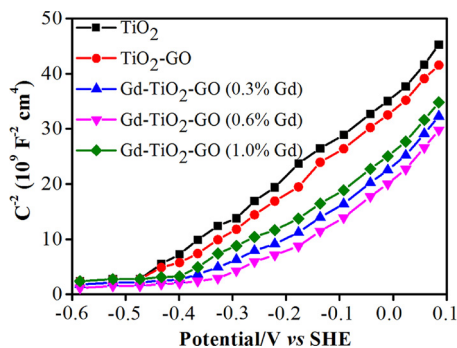

Fig. 15. Mott–Schottky plot of the as–fabricated samples.

vs. SCE, and are *ca.* –0.24, –0.19, –0.12, –0.10 and –0.14 V *vs.* normal hydrogen electrode (NHE) (NHE = SCE + 0.24 V), respectively. Compared to the pure TiO$_2$, E_{fb} of Gd–TiO$_2$–GO (0.6% Gd) was shifted negatively by 0.14 V, which revealed that a higher quasi–Fermi energy level was observed by doping with 0.6% Gd^{3+} ion [102]. With the hypothesis that the E_{fb} lied at the same potential with that of CB edge [103], the VB level could be obtained by subtracting the bandgap energy from the CB level. The VB positions of pure TiO$_2$, TiO$_2$–GO, Gd–TiO$_2$–GO (0.3% Gd), Gd–TiO$_2$–GO (0.6% Gd) and Gd–TiO$_2$–GO (1.0% Gd) were determined to be 2.92, 2.71, 2.66, 2.63 and 2.68 eV *vs.* NHE, respectively. The band alignment of the as–fabricated photocatalysts were schematically shown in Fig. 16.

The Fermi energy level shifted to a more positive potential for Gd–TiO$_2$–GO (0.3% Gd), Gd–TiO$_2$–GO (0.6% Gd) and Gd–TiO$_2$–GO (1.0% Gd) compared with the pure TiO$_2$. This induces a shorter transfer pathway for the photogenerated electrons [104]. As a result, the electronic structure of Gd–TiO$_2$–GO (0.6% Gd) was anticipated to expedite the transfer of charge carriers, and hence, enhance its photoactivity.

3.16. Possible reaction mechanism

To elucidate the improved photoactivity of Gd–TiO$_2$–GO nanocomposite, their CB and VB potentials were evaluated using the empirical formula given in Eqs. (15) and (16) [105]:

$$E_{VB} = \chi - E_c + 0.5E_g \tag{15}$$

$$E_{CB} = E_{VB} - E_g \tag{16}$$

where E_{CB} and E_{VB} are the CB and VB edge potential, respectively. The χ, E_g and E_c represent the electronegativity of TiO$_2$ (χ = 5.81 eV) [106], the estimated bandgap of TiO$_2$, and the standard electrode potential on the hydrogen scale (about 4.5 eV), respectively. Based on Eqs. (15) and (16), the VB and CB potentials of TiO$_2$ were calculated as 2.89 and –0.27 eV, respectively. The potential of GO sheet had been estimated as –0.08 eV (*vs.* NHE) [107]. This study revealed that in the photocatalytic reaction process of Gd–TiO$_2$–GO, O$_2^{-\cdot}$ radical anion and HO$^{\cdot}$ radical were the main reactive oxidising species. Therefore, based on the experimental results and analysis, a schematic mechanism of improved photodegradation of IC dye under visible light irradiation by Gd–TiO$_2$–GO was proposed, as shown in Fig. 17.

When TiO$_2$ was irradiated by a photon of energy greater than or equal to its bandgap energy, electrons in the VB of TiO$_2$ can be photoexcited to the CB after the photogeneration of electrons and holes. The fate of these photogenerated electrons and holes rely on their recombination probability or independent interactions with other molecules in an aqueous solution [108]. The photoexcited electrons in TiO$_2$ were transferred across the Gd–TiO$_2$–GO interface to the CB of GO sheets (GO serve as electron acceptor) *via* the Gd^{3+} ion (Gd^{3+} ion serves as an electrical path for the photogenerated electrons in TiO$_2$) with the holes left on the VB of TiO$_2$, since the CB potential of TiO$_2$ (–0.27 eV) was more negative compared with GO sheets (–0.08 eV). Therefore, the coupling of TiO$_2$ with GO sheets and Gd^{3+} ion could effectively decrease the charge carrier recombination rate to improve the interfacial charge migration efficiency, as observed in the PL spectra (Fig. 13b). Then, the excited electrons stored in GO sheets cannot be
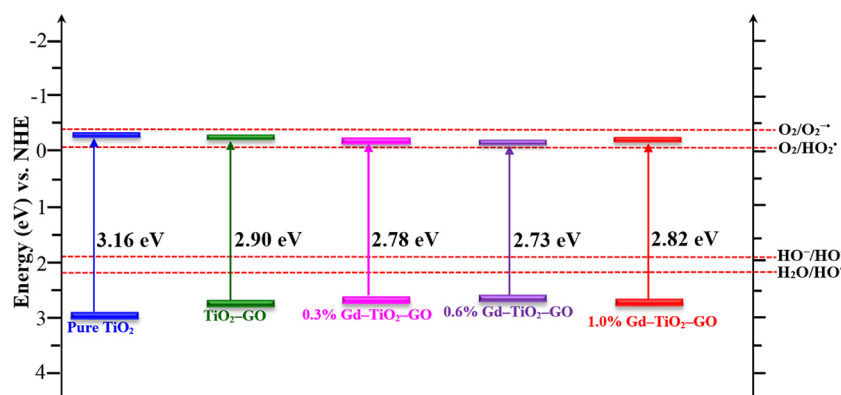

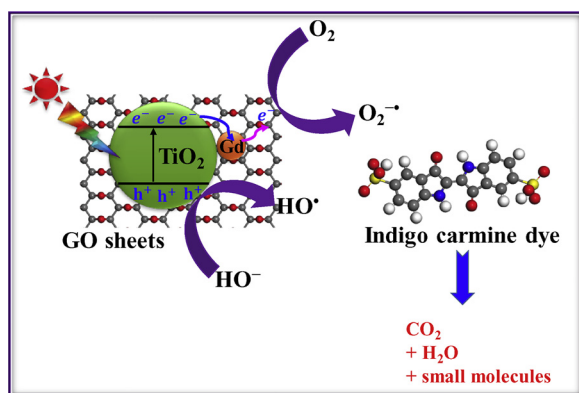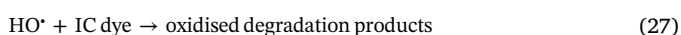**Fig. 16.** The band alignment of the as–fabricated samples.

Fig. 17. The proposed photodegradation mechanism of IC dye by Gd–TiO$_2$–GO photocatalyst under light irradiation.

trapped by the O$_2$ molecules to generate reactive O$_2^{-\cdot}$ radical anion owing to the less CB potential (–0.08 eV) in comparison with that of [E°(O$_2$/O$_2^{-\cdot}$) = –0.33 V] [109], but can react with hydrogen peroxide to form peroxyl radical (HO$_2^{\cdot}$) [E°(O$_2$/HO$_2^{\cdot}$) = –0.05 V]. The generated O$_2^{-\cdot}$ and HO$_2^{\cdot}$) radicals could further combine with electrons and holes to form HO$^{\cdot}$ radicals, thereby improving the degradation efficiency of IC dye. However, the photogenerated holes directly shifted to the TiO$_2$ surface were scavenged by $-$OH anion or H$_2$O molecules to form HO$^{\cdot}$ radicals due to the more positive VB potential (2.89 eV) than that of water oxidation [E°($^{\cdot}$OH/OH) = 2.38 V]. This produced HO$^{\cdot}$ radicals are very strong oxidising agents and could transform the IC dye into oxidised by–products. The major reaction steps from the IC degradation process were described based on Eqs. (17)–(27):

$$TiO_2 + h\nu \rightarrow TiO_2 \; (e^- + h^+) \tag{17}$$

$$TiO_2 \; (e^-) + Gd \rightarrow TiO_2 + Gd \; (e^-) \tag{18}$$

$$Gd \; (e^-) + GO \rightarrow Ce + GO \; (e^-) \tag{19}$$

$$GO \; (e^-) + O_2 \rightarrow GO + O_2^{-\cdot} \tag{20}$$

$$O_2^{-\cdot} + H_2O \rightarrow HO^{\cdot} \tag{21}$$

$$O_2^{-\cdot} + H^+ \rightarrow HO_2^{\cdot} \tag{22}$$

$$2HO_2^{\cdot} \rightarrow H_2O_2 + O_2 \tag{23}$$

$$H_2O_2 + O_2^{-\cdot} \rightarrow HO^{\cdot} + HO^- + O_2 \tag{24}$$

$$TiO_2 \; (h^+) + H_2O \rightarrow HO^{\cdot} + H^+ \tag{25}$$

$$TiO_2 (h^+) + HO^- \rightarrow TiO_2 + HO^{\cdot} \tag{26}$$

$$HO^{\cdot} + IC \; dye \rightarrow oxidised \; degradation \; products \tag{27}$$

Due to the enhanced charge carrier mobility of GO sheets and high BET surface area, suitable integration of Gd^{3+} ion might lead to a hybrid nanocomposite having a high photodegradation performance.

4. Conclusions

Developing and synthesising hybrid visible light active materials is a vital research area in photocatalysis. A sol–gel method was used to fabricate a series of visible–light–driven Gd–TiO$_2$–GO nanocomposites with 0.3, 0.6 and 1.0 wt% of Gd. To access the mechanism of the photocatalytic enhancement, electronic property, interfacial interaction, charge separation and transfer rate of Gd–TiO$_2$–GO nanocomposite were studied using a hybrid DFT calculation. The photocatalytic activity of the prepared samples was considered both in the dark and visible light active IC dye. The Gd–TiO$_2$–GO nanocomposite showed enhanced degradation activity than the pure TiO$_2$ and TiO$_2$–GO. The improved activity was due to the reduced recombination rate of

charged carriers, as confirmed by photoluminescence analysis. The photodegradation rate of Gd–TiO$_2$–GO (0.6% Gd) was 14.19–fold, 4.15–fold, 1.37–fold and 1.72–fold higher than pure TiO$_2$, TiO$_2$–GO, Gd–TiO$_2$–GO (0.3% Gd) and Gd–TiO$_2$–GO (1.0% Gd), respectively, signifying that 0.6 wt% was the optimal Gd content. The results obtained suggested that both holes and HO$^{\cdot}$ radicals were actively involved in the degradation of IC dye. The TOC analysis revealed a high degree of complete mineralisation. Furthermore, the Gd–TiO$_2$–GO (0.6% Gd) nanocomposite displayed an efficient recyclability and stability *via* simulated light irradiation. The smaller effective mass indicated that the charge carriers in the nanocomposites were easy to migrate in the opposite direction, resulting in a suitable type–II band alignment. In view of the first–principles calculation, a change in CB energy level and variation of different orbitals (C 2p and Gd 5d) to the CB in the nanocomposite favour electron transfer. The theoretical studies revealed that Gd^{3+} ion might serve as a charge carrier mediator to draw electrons from Gd–TiO$_2$ to GO sheets, resulting in an enhanced electron accumulation and separation in the GO sheets and decreased the work function. This study gives the underlying photocatalysis mechanism of Gd–TiO$_2$–GO nanocomposite and offers a valuable reference for future design of TiO$_2$–based photocatalyst with high performance in environmental remediation.

References

[1] S. Malato, P. Fernández–Ibáñez, M.I. Maldonado, J. Blanco, W. Gernjak, Catal. Today 147 (2009) 1–59.
[2] M.N. Chong, B. Jin, C.W. Chow, C. Saint, Water Res. 44 (2010) 2997–3027.
[3] A. Ameta, R. Ameta, M. Ahuja, Sci. Rev. Chem. Commun. 3 (2013) 172–180.
[4] I. Oller, S. Malato, J. Sánchez–Pérez, Sci. Total Environ. 409 (2011) 4141–4166.
[5] E.S. Agorku, M.A. Mamo, B.B. Mamba, A.C. Pandey, A.K. Mishra, J. Porous Mater. 22 (2015) 47–56.
[6] A. Fakhru'l–Razi, A. Pendashteh, L.C. Abdullah, D.R.A. Biak, S.S. Madaeni, Z.Z. Abidin, J. Hazard. Mater. 170 (2009) 530–551.
[7] F. Fresno, R. Portela, S. Suárez, J.M. Coronado, J. Mater. Chem. A 2 (2014) 2863–2884.
[8] F. Chen, X. Yang, H.K. Mak, D.W. Chan, Build. Environ. 45 (2010) 1747–1754.
[9] A. Asiagwu, Int. J. Res. Rev. Appl. Sci. 13 (2012) 617–625.
[10] M. Stucchi, C. Bianchi, C. Pirola, G. Vitali, G. Cerrato, S. Morandi, C. Argirusis, G. Sourkouni, P. Sakkas, V. Capucci, Appl. Catal. B 178 (2015) 124–132.
[11] X. Feng, K. Shankar, O.K. Varghese, M. Paulose, T.J. Latempa, C.A. Grimes, Nano Lett. 8 (2008) 3781–3786.
[12] A. Weir, P. Westerhoff, L. Fabricius, K. Hristovski, N. Von Goetz, Environ. Sci. Technol. 46 (2012) 2242–2250.
[13] H. Lee, H.C. Leventis, S.J. Moon, P. Chen, S. Ito, S.A. Haque, T. Torres, F. Nüesch, T. Geiger, S.M. Zakeeruddin, Adv. Funct. Mater. 19 (2009) 2735–2742.
[14] A.–W. Xu, Y. Gao, H.–Q. Liu, J. Catal. 207 (2002) 151–157.
[15] U. Siemon, D. Bahnemann, J.J. Testa, D. Rodríguez, M.I. Litter, N. Bruno, J. Photochem. Photobiol. A: Chem. 148 (2002) 247–255.
[16] E.S. Agorku, B.B. Mamba, A.C. Pandey, A.K. Mishra, J. Nanomater. 2014 (2014) 1–11.
[17] Ž. Antić, R.M. Krsmanović, M.G. Nikolić, M. Marinović–Cincović, M. Mitrić, S. Polizzi, M.D. Dramićanin, Mater. Chem. Phys. 135 (2012) 1064–1069.
[18] S.M. Kumaran, R. Gopalakrishnan, J. Sol–Gel Sci. Technol. 62 (2012) 193–200.
[19] K.–Q. Lu, Y. Chen, X. Xin, Y.–J. Xu, Appl. Catal. B 224 (2018) 424–432.
[20] K.–Q. Lu, X. Xin, N. Zhang, Z.–R. Tang, Y.–J. Xu, J. Mater. Chem. A 6 (2018) 4590–4604.
[21] K.–Q. Lu, L. Yuan, X. Xin, Y.–J. Xu, Appl. Catal. B 226 (2018) 16–22.
[22] N. Khalid, E. Ahmed, Z. Hong, M. Ahmad, Appl. Surf. Sci. 263 (2012) 254–259.
[23] Z. Wang, B. Huang, Y. Dai, Y. Liu, X. Zhang, X. Qin, J. Wang, Z. Zheng, H. Cheng, CrystEngComm 14 (2012) 1687–1692.
[24] C. Han, N. Zhang, Y.–J. Xu, Nano Today 11 (2016) 351–372.

[25] N. Zhang, M.–Q. Yang, S. Liu, Y. Sun, Y.–J. Xu, Chem. Rev. 115 (2015) 10307–10377.
[26] Y. Zhang, Z.–R. Tang, X. Fu, Y.–J. Xu, ACS Nano 4 (2010) 7303–7314.
[27] J. Low, J. Yu, M. Jaroniec, S. Wageh, A.A. Al-Ghamdi, Adv. Mater. 29 (2017) 1601694.
[28] K. Lv, S. Fang, S. Si, Y. Xia, W. Ho, M. Li, Appl. Surf. Sci. 391 (2017) 218–227.
[29] M. Zhu, Y. Muhammad, P. Hu, B. Wang, Y. Wu, X. Sun, Z. Tong, Z. Zhao, Appl. Catal. B 232 (2018) 182–193.
[30] K. Woan, G. Pyrgiotakis, W. Sigmund, Adv. Mater. 21 (2009) 2233–2239.
[31] S.O.–B. Oppong, W.W. Anku, S.K. Shukla, E.S. Agorku, P.P. Govender, J. Sol–Gel Sci. Technol. 80 (2016) 38–49.
[32] S.J. Clark, M.D. Segall, C.J. Pickard, P.J. Hasnip, M.I. Probert, K. Refson, M.C. Payne, Z. Kristallogr. Cryst. Mater. 220 (2005) 567–570.
[33] Materials Studio Simulation Environment, Release 2016, Accelrys Software Inc., San Diego, CA, 2016.
[34] J.P. Perdew, K. Burke, M. Ernzerhof, Phys. Rev. Lett. 77 (1996) 3865–3868.
[35] D. Vanderbilt, Phys. Rev. B 41 (1990) 7892–7895.
[36] B.G. Pfrommer, M. Côté, S.G. Louie, M.L. Cohen, J. Comput. Phys. 131 (1997) 233–240.
[37] H.J. Monkhorst, J.D. Pack, Phys. Rev. B 13 (1976) 5188–5192.
[38] J.P. Perdew, Int. J. Quantum Chem. 30 (1986) 451–451.
[39] J. Heyd, G.E. Scuseria, M. Ernzerhof, J. Chem. Phys. 118 (2003) 8207–8215.
[40] Y. Liang, Y. Li, H. Wang, J. Zhou, J. Wang, T. Regier, H. Dai, Nat. Mater. 10 (2011) 780–786.
[41] D.C. Marcano, D.V. Kosynkin, J.M. Berlin, A. Sinitskii, Z. Sun, A. Slesarev, L.B. Alemany, W. Lu, J.M. Tour, ACS Nano 4 (2010) 4806–4814.
[42] Y. Gao, X. Pu, D. Zhang, G. Ding, X. Shao, J. Ma, Carbon 50 (2012) 4093–4101.
[43] S. Chatrchyan, V. Khachatryan, A.M. Sirunyan, A. Tumasyan, W. Adam, E. Aguilo, T. Bergauer, M. Dragicevic, J. Erö, C. Fabjan, Phys. Lett. B 716 (2012) 30–61.
[44] K. Dai, L. Lu, Q. Liu, G. Zhu, Q. Liu, Z. Liu, Dalton Trans. 43 (2014) 2202–2210.
[45] M. Wojtoniszak, X. Chen, R.J. Kalenczuk, A. Wajda, J. Łapczuk, M. Kurzewski, M. Drozdzik, P.K. Chu, E. Borowiak–Palen, Colloids Surf. B: Binterfaces 89 (2012) 79–85.
[46] J.–H. Choy, H.–C. Lee, H. Jung, S.–J. Hwang, J. Mater. Chem. 11 (2001) 2232–2234.
[47] Y. Zhou, W. Wu, K. Qiu, Waste Manage. (Oxf.) 30 (2010) 2299–2304.
[48] P. Zhang, C. Shao, M. Zhang, Z. Guo, J. Mu, Z. Zhang, X. Zhang, Y. Liu, J. Hazard. Mater. 217 (2012) 422–428.
[49] H. Teymourian, A. Salimi, S. Firoozi, A. Korani, S. Soltanian, Electrochim. Acta 143 (2014) 196–206.
[50] K. Gurushantha, K. Anantharaju, L. Renuka, S. Sharma, H. Nagaswarupa, S. Prashantha, Y. Vidya, H. Nagabhushana, RSC Adv. 7 (2017) 12690–12703.
[51] X. Yu, J. Liu, Y. Yu, S. Zuo, B. Li, Carbon 68 (2014) 718–724.
[52] D. Luo, G. Zhang, J. Liu, X. Sun, J. Phys. Chem. C 115 (2011) 11327–11335.
[53] B. Panigrahy, S. Srivastava, New J. Chem. 40 (2016) 3370–3384.
[54] A.C. Ferrari, J. Robertson, Phys. Rev. B 61 (2000) 14095.
[55] P. Wang, J. Wang, X. Wang, H. Yu, J. Yu, M. Lei, Y. Wang, Appl. Catal. B 132 (2013) 452–459.
[56] S. Verma, H.P. Mungse, N. Kumar, S. Choudhary, S.L. Jain, B. Sain, O.P. Khatri, Chem. Commun. 47 (2011) 12673–12675.
[57] S. Narksitipan, S. Thongtem, Ferroelectr. Lett. Sect. 41 (2014) 94–99.
[58] Y.–Z. Zheng, Y.–Y. Xu, H.–B. Fang, Y. Wang, X. Tao, RSC Adv. 5 (2015) 103790–103796.
[59] E. Barborini, A.M. Conti, I. Kholmanov, P. Piseri, A. Podestà, P. Milani, C. Cepek, O. Sakho, R. Macovez, M. Sancrotti, Adv. Mater. 17 (2005) 1842–1846.
[60] A. Primo, T. Marino, A. Corma, R. Molinari, H. Garcia, J. Am. Chem. Soc. 133 (2011) 6930–6933.
[61] P. Sudhagar, K. Asokan, E. Ito, Y.S. Kang, Nanoscale 4 (2012) 2416–2422.
[62] X. Chen, L. Liu, Y.Y. Peter, S.S. Mao, Science 331 (2011) 746–750.
[63] G. Wang, H. Wang, Y. Ling, Y. Tang, X. Yang, R.C. Fitzmorris, C. Wang, J.Z. Zhang, Y. Li, Nano Lett. 11 (2011) 3026–3033.
[64] J. Tian, S. Liu, Y. Zhang, H. Li, L. Wang, Y. Luo, A.M. Asiri, A.O. Al-Youbi, X. Sun, Inorg. Chem. 51 (2012) 4742–4746.
[65] J. Tauc, Mater. Res. Bull. 3 (1968) 37–46.
[66] B.E. Sernelius, K.–F. Berggren, Z.–C. Jin, I. Hamberg, C. Granqvist, Phys. Rev. B 37 (1988) 10244.
[67] E. Davis, N. Mott, Philos. Mag. 22 (1970) 0903–0922.
[68] N. Tian, Y. Zhang, X. Li, K. Xiao, X. Du, F. Dong, G.I. Waterhouse, T. Zhang, H. Huang, Nano Energy 38 (2017) 72–81.
[69] B.K. Vijayan, N.M. Dimitrijevic, D. Finkelstein–Shapiro, J. Wu, K.A. Gray, ACS Catal. 2 (2012) 223–229.
[70] J. Rengifo–Herrera, K. Pierzchała, A. Sienkiewicz, L. Forro, J. Kiwi, C. Pulgarin, Appl. Catal. B 88 (2009) 398–406.
[71] A.–L. Cheng, Y.–K. Kang, Z. Chen, C.–J. Tsao, S. Qin, J.S. Kim, R. Luo, J. Feng, S. Ye, T.–S. Yang, Lancet Oncol. 10 (2009) 25–34.
[72] U. Mallick, C. Harmer, B. Yap, J. Wadsley, S. Clarke, L. Moss, A. Nicol, P.M. Clark, K. Farnell, R. McCready, New Engl. J. Med. 366 (2012) 1674–1685.
[73] J. Yu, M.A. Vodyanik, K. Smuga–Otto, J. Antosiewicz–Bourget, J.L. Frane, S. Tian, J. Nie, G.A. Jonsdottir, V. Ruotti, R. Stewart, Science 318 (2007) 1917–1920.
[74] H. Yang, J. Li, L. Yu, B. Huang, Y. Ma, Y. Dai, J. Mater. Chem. A 6 (2018) 4161–4166.
[75] J. Choi, P. Sudhagar, P. Lakshmipathiraj, J.W. Lee, A. Devadoss, S. Lee, T. Song, S. Hong, S. Eito, C. Terashima, RSC Adv. 4 (2014) 11750–11757.
[76] R. Shannon, Acta Crystallogr. Sect. A 32 (1976) 751–767.
[77] L. Xu, W.–Q. Huang, L.–L. Wang, G.–F. Huang, ACS Appl. Mater. Interfaces 6 (2014) 20350–20357.
[78] F. Opoku, K.K. Govender, C.G.C.E. van Sittert, P.P. Govender, Carbon 136 (2018) 187–195.
[79] F. Opoku, K.K. Govender, C.G.C.E. van Sittert, P.P. Govender, New J. Chem. 41 (2017) 8140–8155.
[80] D. Ren, H. Li, X. Cheng, Solid State Commun. 223 (2015) 54–59.
[81] B. Modak, S.K. Ghosh, J. Phys. Chem. C 119 (2015) 7215–7224.
[82] H. Li, L. Chen, S. Liu, C. Li, J. Meng, Z. Wang, Mater. Sci.–Pol. 33 (2015) 549–554.
[83] L. Shao, J. Li, Y. Zhang, S. Gong, H. Zhang, Y. Wang, J. Mater. Chem. A 2 (2014) 14173–14180.
[84] D.O. Scanlon, C.W. Dunnill, J. Buckeridge, S.A. Shevlin, A.J. Logsdail, S.M. Woodley, C.R.A. Catlow, M.J. Powell, R.G. Palgrave, I.P. Parkin, G.W. Watson, T.W. Keal, P. Sherwood, A. Walsh, A.A. Sokol, Nat. Mater. 12 (2013) 798–801.
[85] S. Gharedaghi, S. Kimiagar, S. Safa, Phys. Status Solidi A 215 (2018) 1700618.
[86] E. Mete, D. Uner, O. Gülseren, Ş. Ellialtıoğlu, Phys. Rev. B 79 (2009) 125418.
[87] H. Zhang, L. Liu, Z. Zhou, RSC Adv. 2 (2012) 9224–9229.
[88] J. Zhang, P. Zhou, J. Liu, J. Yu, Phys. Chem. Chem. Phys. 16 (2014) 20382–20386.
[89] Beer, Ann. Phys. 162 (1852) 78–88.
[90] M. Pelaez, N.T. Nolan, S.C. Pillai, M.K. Seery, P. Falaras, A.G. Kontos, P.S. Dunlop, J.W. Hamilton, J.A. Byrne, K. O'shea, Appl. Catal. B 125 (2012) 331–349.
[91] C. Ran, M. Wang, W. Gao, J. Ding, Y. Shi, X. Song, H. Chen, Z. Ren, J. Phys. Chem. C 116 (2012) 23053–23060.
[92] X.–Y. Zhang, H.–P. Li, X.–L. Cui, Y. Lin, J. Mater. Chem. 20 (2010) 2801–2806.
[93] W. Gao, M. Wang, C. Ran, X. Yao, H. Yang, J. Liu, D. He, J. Bai, Nanoscale 6 (2014) 5498–5508.
[94] N.K. Eswar, S.A. Singh, G. Madras, Chem. Eng. J. 332 (2018) 757–774.
[95] M. Long, W. Cai, J. Cai, B. Zhou, X. Chai, Y. Wu, J. Phys. Chem. B 110 (2006) 20211–20216.
[96] J.–G. Yu, H.–G. Yu, B. Cheng, X.–J. Zhao, J.C. Yu, W.–K. Ho, J. Phys. Chem. B 107 (2003) 13871–13879.
[97] T. Wang, Z.–y. Xu, L.–g. Wu, B.–r. Li, M.–x. Chen, S.–y. Xue, Y.–c. Zhu, J. Cai, RSC Adv. 7 (2017) 31921–31929.
[98] X. Wang, J.–G. Li, H. Kamiyama, Y. Moriyoshi, T. Ishigaki, J. Phys. Chem. B 110 (2006) 6804–6809.
[99] A. Charanpahari, S. Umare, R. Sasikala, Appl. Surf. Sci. 282 (2013) 408–414.
[100] Y. Chai, L. Wang, J. Ren, W.–L. Dai, Appl. Surf. Sci. 324 (2015) 212–220.
[101] Y. Bai, L. Ye, T. Chen, L. Wang, X. Shi, X. Zhang, D. Chen, ACS Appl. Mater. Interfaces 8 (2016) 27661–27668.
[102] Y. Duan, N. Fu, Q. Liu, Y. Fang, X. Zhou, J. Zhang, Y. Lin, J. Phys. Chem. C 116 (2012) 8888–8893.
[103] J. Premkumar, Chem. Mater. 16 (2004) 3980–3981.
[104] L. Ge, C. Han, J. Liu, Y. Li, Appl. Catal. A 409 (2011) 215–222.
[105] A.H. Nethercot Jr, Phys. Rev. Lett. 33 (1974) 1088–1091.
[106] Y. Xu, M.A. Schoonen, Am. Mineral. 85 (2000) 543–556.
[107] Q. Xiang, J. Yu, M. Jaroniec, Nanoscale 3 (2011) 3670–3678.
[108] N. Kumar, S.S. Ray, J.C. Ngila, New J. Chem. 41 (2017) 14618–14626.
[109] Y. Ide, F. Liu, J. Zhang, N. Kawamoto, K. Komaguchi, Y. Bando, D. Golberg, J. Mater. Chem. A 2 (2014) 4150–4156.